Available online at www.sciencedirect.com
ScienceDirect
Journal of Sound and Vibration 303 (2007) 78–108
JOURNAL OF SOUND AND VIBRATION
www.elsevier.com/locate/jsvi

# Stability analysis of uniform and non-uniform annular passages conducting incompressible laminar flows for small and large amplitude oscillatory motions of the outer cylinder

A. Mekanik[a,*], M.P. Païdoussis[b]

[a]*Department of Mechanical Engineering, Bu-Ali Sina University, Hamadan, Iran*
[b]*Department of Mechanical Engineering, McGill University, Montreal, Québec, Canada H3A 2K6*

Received 12 March 2006; received in revised form 20 December 2006; accepted 20 December 2006
Available online 7 March 2007

**Abstract**

A computational method is developed involving the simultaneous integration of the Navier–Stokes and structural equations for the purpose of studying the stability of concentric annular passages conducting incompressible laminar flows. It is assumed that one side of the annulus, i.e. the centre-body, is fixed and the outer cylindrical duct is flexibly supported. The outer cylinder is displaced from its equilibrium position and is then released. In this situation, the fluid part of the problem is solved by an accurate method using a three-point backward implicit scheme, followed by a pseudo-time iteration using an artificial compressibility factor. The fluid equations are discretized in space based on a finite-difference formulation and primitive variables, for which stretched staggered grids are used. The resulting equations are cast in delta form and are solved using an ADI scheme. The fluid forces acting on the vibrating cylinder are calculated from the integration of the unsteady pressure and shear stresses resulting from the unsteady primitive variables calculated. The equations of motion of the structure, subjected to the calculated fluid forces are solved using the Runge–Kutta scheme to obtain the displacement of the moving cylinder. The problem is solved: (a) for small-amplitude motions, by means of the so-called mean position (MP) analysis and (b) for large amplitude oscillations of the outer cylinder for which a *time-dependent coordinate transformation* (TDCT) is used to fix the computational domain. Both these approaches (MP and TDCT) are applied to uniform and non-uniform (backstep-shaped) annuli for translational motion of the cylinder. The problem is also solved for (i) rocking motion and uniform annuli and (ii) translational motion for diffuser-shaped annuli, with only MP analysis. When the MP analysis is considered, it is shown that, for translational motion of the outer cylinder, the most stable configuration is that of a uniform geometry and the least stable one is the backward step geometry. For rocking motion in uniform annular geometry, for some system parameters and high enough flow velocity, the outer cylinder can develop flutter (limit-cycle oscillation). The comparison between the results of MP and TDCT analyses for uniform and backstep geometries for translational motion of the cylinder indicates that the outer cylinder is less stable when TDCT is used and the coupled frequency of oscillation is also changed considerably.


*Corresponding author. Tel.: +98 811 8224256; fax: +98 811 8257400.
*E-mail address:* Meka47ir@Yahoo.com (A. Mekanik).

0022-460X/$ - see front matter © 2007 Elsevier Ltd. All rights reserved.
doi:10.1016/j.jsv.2006.12.019

## 1. Introduction

There are many engineering systems involving subsystems in which flexible structures are subjected to annular flow. Examples are control rods in guide tubes, fuel strings in coolant channels, and feedwater spargers, in various types of nuclear reactors [1]; certain types of jet pumps, pistons and valves; thermal shields in nuclear reactors and heat shields in aircraft engines; oil and gas production systems; fiber spinning and wire coating manufacture. A fuller list is given in Ref. [2, Chapter 11]. Such systems are notoriously susceptible to fluid-elastic instabilities and vibration problems, especially when the flow passage is narrow (often referred to as a leakage flow-induced vibration). In Ref. [1], ten practical cases of annular flow-induced-problems are discussed, resulting in damage through wear and outright fracture, and some more in Ref. [2]; refer also to Refs. [3–5]. This explains the interest in the study of motion-induced fluid loading on structures in annular geometries, and on the resultant self-excited motions.

Some work on stability of flexible cylinders in axisymmetrically confined flow was undertaken by Païdoussis et al. [6,7]. Since then, the research effort on this topic, specially applicable to narrow annuli has intensified and a number of interesting papers on the subject may be found in the proceedings of various symposia in this area; see, e.g., Païdoussis and Au-Yang [8,9] and Païdoussis et al. [10]. The first attempts to generate an analytical viscous model for the annular geometry are due to Hobson [11] and Spurr and Hobson [12]. For the sake of simplicity, Hobson considered a rigid cylindrical body, hinged at one point and coaxially positioned in a flow-carrying duct, generally of non-uniform cross-sectional area; he showed that, at sufficiently high flow velocities, oscillatory instability can occur, via a negative damping mechanism. Moreover, the model was capable of dealing, in an approximate manner involving some degree of empiricism, with configurations involving sudden constriction or enlargement in the flow passage. The analysis was extended to predict the dynamical behaviour of an actual fuel assembly oscillating in a channel of arbitrary shape [13]. Measurements of damping forces caused by flow between two concentric cylinders were made by Hobson [14] in which he compared the experimental results with theory by making simple quasi-steady assumptions about the frictional forces acting on the cylinder. It was shown that damping of cylindrical structures due to annular flow arises from inlet or outlet effects and from frictional effects in the annulus, both effects increasing with flow velocity. Also, he found that the damping forces and pressure distribution along the annulus can be well predicted if simple assumptions about the unsteady flow in the annulus are made.

Several approaches have been used by different researchers to conduct theoretical or experimental studies on fluid–structure interactions in very narrow annuli, or on the so-called leakage flows. Among them is the study of Ashurts and Durst [15] on flow-induced vibrations associated with shear-layer-induced flow oscillation in a symmetric, two-dimensional (2-D), plane test-section with a sudden expansion. Parkin and Watson [16] described a physical model for explaining the flow-induced vibration observed in $6^\circ$ and $30^\circ$ annular diffusers, where the centre-body forming the diffuser can move radially. Their model is based on experimental evidence and accounts for both fluid behaviour and structural response. Spurr and Hobson [12] conducted some experiments in which they measured the unsteady forces caused by the flow down an annulus formed between a fixed outer cylinder and a vibrating centre-body and compared the results with those predicted using a linear small perturbation analysis. It was found that the forces are particularly sensitive to the amount of pressure recovery which takes place when the annulus is terminated by an annular diffuser. They also found that high pressure recovery leads to forces on the centre-body which are in phase with its velocity and therefore likely to lead to coupled fluid–structure self-excited vibrations.

Mulcahy [17] obtained closed form solutions for the flow-induced damping (velocity-dependent) and stiffness (displacement-dependent) forces acting on the vibrating walls of a one-dimensional (1-D) leakage-flow channel. His final conclusion was that the minimum conditions necessary for dynamic and static (divergence) instabilities are (i) a pressure loss at the upstream end of the annulus and (ii) a divergent channel with a finite-length throat region.

Hobson and Jedwab [18] studied the effect of eccentricity on the unsteady forces on the centre-body of an annular diffuser. They found that periodic instability can be initiated by increasing the forced vibration amplitude above a frequency-dependent threshold.

Inada and Hayama [19] theoretically and experimentally analyzed the viscous fluid-dynamic forces and the moments acting on the walls of a 1-D, narrow, tapered passage when one wall is vibrating in pure translation

or rotation, or in coupled motion involving both translational and rotational modes. The fluid dynamic mass, damping and stiffness matrices are determined, with the help of which the mechanism of instability generated by the flow through the narrow passage is examined.

A more rigorous, purely analytical potential-flow model was formulated by Mateescu and Païdoussis [20], once again for a rigid centre-body, hinged at one point and coaxially positioned in a flow-carrying conduit. In this inviscid analysis, it was found that there is a critical location of the hinge: if the hinge is situated downstream of that location, then the system may lose stability at sufficiently high flow velocity when the negative fluid-dynamic damping, associated with the motions of the centre-body, overcomes the mechanical damping. It was also found that a divergent flow passage (diffuser) destabilizes the system, whereas a convergent one stabilizes it, which agrees with Hobson's findings.

This rigid-body model was then extended to approximately take into account viscous effects [21]. The principal finding of this work was that viscous effects stabilize the system, and that they become more important as the annulus becomes narrower. In that analysis, an approximate solution of the Navier–Stokes (N–S) equations was obtained. Subsequently, the fluid-dynamic pressures acting on the centre-body in rocking motion were measured and compared with the theoretical ones [22].

In another investigation in which a flexible, as opposed to flexibly mounted, structure was used, the dynamical behaviour of the system of a cylindrical beam with fixed ends subjected to axial flow in a narrow annulus was studied [23]. It was found that, as the annular gap becomes narrower, the system loses stability by divergence at smaller flow velocities, provided the gap size is such that inviscid fluid effects are dominant. For very narrow annuli, however, where viscous forces dominate, this trend is reversed, and further narrowing of the gap has a stabilizing effect on the system.

Further development in this area has been achieved by the use of computational models which involve simultaneous numerical integration of the N–S equations for laminar flow, and the equation of motion of the structure [24]. To this end, a forced vibration of the outer (or inner) cylinder in an annular configuration was considered by Mateescu et al. [25,26], in which the simplified N–S equations were linearized and solved in the annulus and the forces on the walls calculated. An extensive discussion of all previous work in this area may be found in Ref. [2].

The present work has generalized the earlier work by Mateescu et al. (i) by taking more fully into account the nonlinearities in the N–S equations, i.e., considering explicitly the coupling terms on the right-hand sides of the equations and (ii) by extending it to deal with non-uniform annular geometries. To carry out these aims, the N–S equations should be transformed in time (if large amplitude oscillation is considered) and in space; i.e., the physical domain of integration should be transformed into a computational domain, for both the uniform and non-uniform annular geometries. When small amplitude oscillation is considered, which is the case in the first part of the present analysis, transformation of the equations in time is not necessary. In the second part, the *time-dependent coordinate transformation* (TDCT) for larger amplitude oscillations is taken into consideration.

The final goal in this work is the stability analysis of the system, described in Sections 2 and 3. The stability of the structure depends most importantly on the fluid-dynamic damping, although the fluid changes the characteristics of the structure in other ways, e.g., by increasing the effective mass of the system or affecting the effective stiffness of the structure.

The purpose of this work is to integrate simultaneously the N–S and the structural equations and obtain the stability (or instability) criteria for motion of the outer cylinder in a concentric geometry, with either a uniform or a non-uniform annular passage (with a backstep or a diffuser shaped centre-body). The flow is assumed to be laminar; hence, the Reynolds number based on the hydraulic diameter should be less than 3000. The model is fundamentally 3-D, although some 2-D results are also presented. Finally, although the formulation is nonlinear, the stability analysis is linear.

## 2. Mean position analysis (small amplitude oscillation)

The annular configuration considered consists of a centre-body concentrically located in a cylindrical conduit as shown in Fig. 1. For an axially uniform configuration, the radius of the inner cylinder is $hr_i$ and the annular space between the two cylinders is $h$; thus the radius of the outer cylinder is $hr_o = hr_i + h$, as shown in

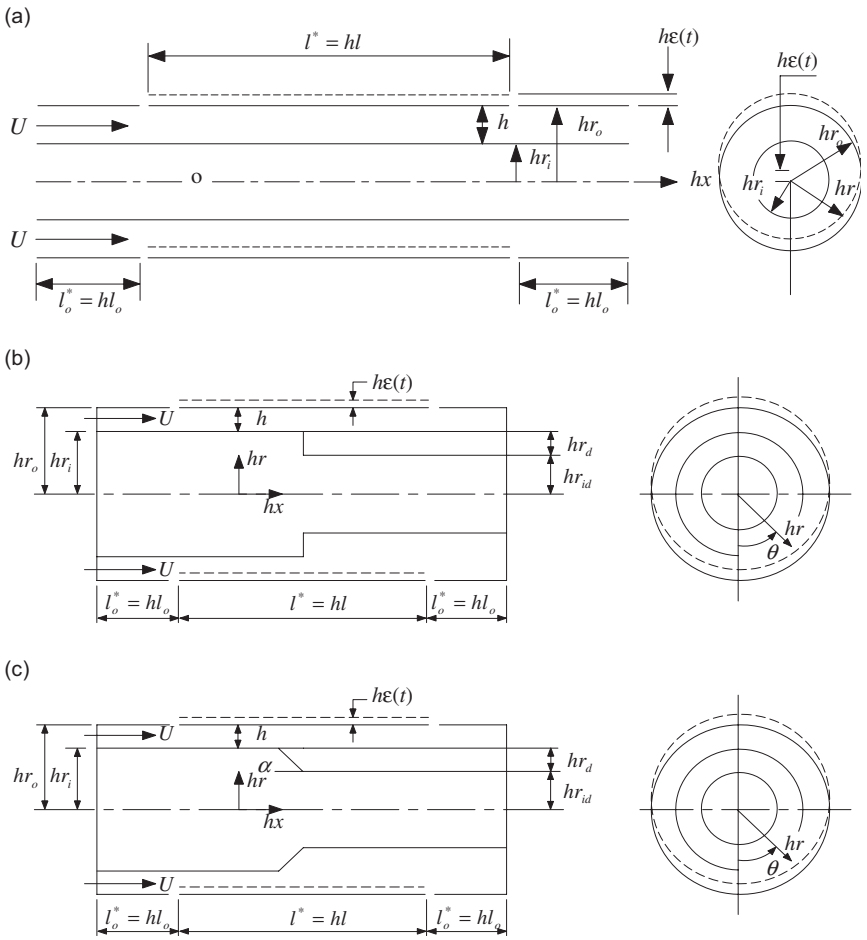


Fig. 1. Geometrical representation of the annular passages under consideration: (a) uniform annular flow, (b) non-uniform annular flow with backstep, (c) non-uniform annular flow with diffuser section. The central portion of the outer cylinder, $l^* = hl$, executes transverse translational oscillation in the longitudinal plane $\theta = 0$.

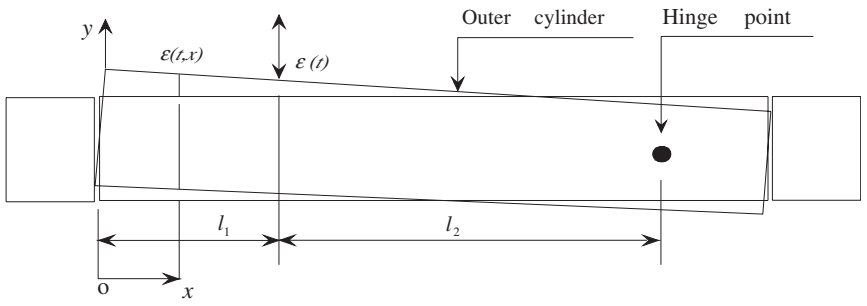


Fig. 2. Schematic representation of the geometry of the outer cylinder during rocking motion, used for boundary velocity calculation.

Fig. 1(a). The centre-body is immersed in either quiescent fluid or a steady laminar flow. It is generally the outer cylinder, which is forced to execute oscillatory motion, while the inner cylinder is fixed. The total length of the outer cylinder is divided into three parts. The upstream and downstream parts of variable length $l_o^* = hl_o$ are kept stationary. The central portion of the cylinder, $l^* = hl$, executes oscillatory motions (either translational as in Fig. 1 or rocking around a fixed hinge as shown in Fig. 2). The radii of $hr_i$ and $hr_o$ as well as

the lengths of the fixed upstream and downstream portions and oscillating cylinder are variable. The annular widths downstream of the backstep or diffuser section are assumed to be appropriately larger than the corresponding upstream section (Figs. 1(b) and (c)); moreover, the angle $\alpha$ of the diffuser section (Fig. 1(c)) is variable. Different values can be used for the flow velocity $U$, including $U = 0$, the amplitude of oscillation $\varepsilon$ (refer to Eq. (13)), and the frequency of oscillation $f$ of the central part of the outer cylinder.

The translational and rocking motions of the outer cylinder take place in a given plane of symmetry. The oscillating part of the outer cylinder is rigid but flexibly supported, by a spring with effective stiffness $K$ and a dashpot with damping coefficient $C$, not shown in the figures. For the purpose of evaluating the effect of fluid damping on the structure, the structural damping $C$ is neglected.

For all systems under consideration it is assumed that the outer cylinder is displaced by a distance $he(t)$ and then released. Due to the oscillation of the outer cylinder, fluid forces are generated which interact with the structure; the final result of this fluid–structure interaction is the dynamical behaviour of the cylinder (e.g., whether it remains stable or becomes unstable), which is the main topic of this work. Before this goal is reached, the fluid forces should be determined by solving the unsteady N–S equations in non-dimensional form (which is applicable to incompressible fluid flow in the laminar regime) in the annular region. In the geometry considered, because of the existence of the rigid immobile segments upstream and downstream of the oscillating segment of the system, no end conditions need explicitly be taken into account in the formulation. Local discontinuities between the moving and immobile segments are taken care of by the numerical scheme; for more explanation refer to Ref. [27].

### 2.1. Solution of the flow field

In this analysis, the viscosity and density are assumed to remain constant. Thus, the continuity and N–S equations, without body forces, are expressed in dimensional form as

$$\nabla^* \cdot \mathbf{V}^* = 0, \quad \frac{\partial \mathbf{V}^*}{\partial t^*} + \nabla^* \cdot (\mathbf{V}^* \mathbf{V}^*) = -\frac{1}{\rho^*} \nabla^* p^* + \nu^* \nabla^{*2} \mathbf{V}^*, \tag{1,2}$$

respectively, where $\mathbf{V}^*$ is the velocity vector, $t^*$ the time, $\rho^*$ the density, $\nu^*$ the kinematic viscosity, and $p^*$ the pressure, where the asterisk denotes a dimensional quantity.[1] In order to generalize the present problem, it is convenient to define the following non-dimensional parameters:

$$\begin{aligned} &x = x^*/h, \quad r = r^*/h, \quad t = t^* U/h, \quad \omega = \omega^* h/U, \\ &u = u^*/U, \quad v = v^*/U, \quad w = w^*/U, \quad \mathbf{V} = \mathbf{V}^*/U, \\ &p = (p^* - p^*_\infty)/(\rho^* U^2), \quad \mathrm{Re} = hU/\nu^* = \tfrac{1}{2}\mathrm{Re}_{D_h}, \quad l = l^*/h, \end{aligned}$$

where $U$ is the reference velocity and $\mathrm{Re}_{D_h}$ the Reynolds number based on the hydraulic diameter of the annulus. Using these parameters, one can write Eqs. (1) and (2) as

$$\nabla \cdot \mathbf{V} = 0, \quad \frac{\partial \mathbf{V}}{\partial t} + \nabla \cdot (\mathbf{V}\,\mathbf{V}) = -\nabla p + \frac{1}{\mathrm{Re}} \nabla^2 \mathbf{V} \tag{3,4}$$

and, in compact form, Eq. (4) is re-written as

$$\frac{\partial \mathbf{V}}{\partial t} + \mathbf{G}(\mathbf{V}, p) = \mathbf{0}, \tag{5}$$

where $\mathbf{V} = [u, v, w]^{\mathrm{T}}$ and $\mathbf{G}(\mathbf{V}, p) = [G_u(u, v, w, p), G_v(u, v, w, p), G_w(u, v, w, p)]^{\mathrm{T}}$. The continuity equation and, as an example, the $G_u$ component of $\mathbf{G}(\mathbf{V}, p)$ in cylindrical coordinates are given by

$$\nabla \cdot \mathbf{V} = \frac{\partial u}{\partial x} + \frac{\partial v}{\partial r} + \frac{1}{r}\frac{\partial w}{\partial \theta} = 0, \tag{6}$$

[1]The length ($h$) and velocity ($U$) scales, however, which will disappear after non-dimensionalization are given without an asterisk.

$$G_u(u,v,w,p)=\frac{\partial(uu)}{\partial x}+\frac{1}{r}\frac{\partial(rvu)}{\partial r}+\frac{1}{r}\frac{\partial(wu)}{\partial\theta}+\frac{\partial p}{\partial x}-\frac{1}{\mathrm{Re}}\left[\frac{\partial^2 u}{\partial x^2}+\frac{1}{r}\frac{\partial}{\partial r}\left(r\frac{\partial u}{\partial r}\right)+\frac{1}{r^2}\frac{\partial^2 u}{\partial\theta^2}\right]. \tag{7}$$

The numerical solution of Eqs. (5) and (6) is obtained by using a three-point backward implicit scheme for the real-time discretization and central differencing based on a stretched staggered grid in spatial discretization as

$$\frac{3\mathbf{V}^{n+1}-4\mathbf{V}^n+\mathbf{V}^{n-1}}{2\Delta t}+\mathbf{G}^{n+1}=\mathbf{0}, \tag{8}$$

where $\Delta t$ is the real time step and $\mathbf{G}^{n+1}=\mathbf{G}(\mathbf{V}^{n+1},p^{n+1})$. This equation can be expressed together with Eq. (6) as

$$\mathbf{V}^{n+1}+\beta\mathbf{G}^{n+1}=\mathbf{E}^n,\quad \nabla\cdot\mathbf{V}^{n+1}=0, \tag{9,10}$$

where $\beta=\frac{2}{3}\Delta t$, $\mathbf{E}^n=\frac{1}{3}(4\mathbf{V}^n-\mathbf{V}^{n-1})$.

In a forced-vibration unsteady flow problem, the known velocity $\mathbf{V}_b^{n+1}$ of a moving boundary is imposed as a boundary condition. Since small-amplitude oscillation is considered here, the boundary conditions are imposed at the *mean position* of the outer cylinder, Fig. 3(a). Therefore, the boundary conditions associated with the geometries of Fig. 1 are given on the fixed inner cylinder $r=r_i$ as

$$v_w(r_i,\theta,t)=0,\quad w_w(r_i,\theta,t)=0 \tag{11}$$

due to the no-slip condition, and on the moving outer cylinder $r_o=r_i+1$ as

$$v_w(r_o,\theta,t)=[\mathrm{d}e_w(t)/\mathrm{d}t]\cos\theta,\quad w_w(r_o,\theta,t)=-[\mathrm{d}e_w(t)/\mathrm{d}t]\sin\theta, \tag{12}$$

$$e_w(t)=-\varepsilon\cos\omega t \tag{13}$$

with $\varepsilon$ as the *non-dimensional amplitude* and $\omega$ is the *circular frequency of the oscillation*. The spatial discretization uses central differencing based on a stretched staggered grid; hence, there is no need for the pressure to be defined at the fixed or moving boundaries.

The solution of Eqs. (9) and (10) is obtained by using an iterative pseudo-time [28] relaxation method with artificial compressibility [29], via which the equations are replaced by

$$\frac{\partial\hat{\mathbf{V}}}{\partial\tau}+\hat{\mathbf{V}}+\beta\hat{\mathbf{G}}=\mathbf{E}^n,\quad \delta\left(\frac{\partial\hat{p}}{\partial\tau}\right)+\nabla\cdot\hat{\mathbf{V}}=0, \tag{14,15}$$

where $\tau$ is the *pseudo-time* which is distinguishable from *real time* $t$, and $\delta$ is the *artificial compressibility* coefficient; $\hat{\mathbf{V}}(\tau)$ and $\hat{p}(\tau)$ denote the pseudo-time values of the velocity and pressure between real-time levels $t^n$ and $t^{n+1}$.

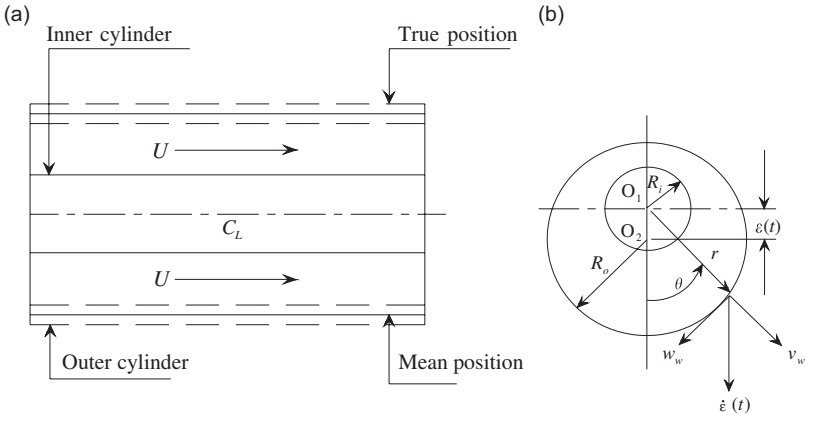


Fig. 3. (a) Schematic diagram indicating the mean and true maximum and minimum positions of the outer cylinder during oscillations. (b) Cross-sectional view of the annular space during oscillation (exaggerated amplitude). The boundary conditions are applied either at the mean position or on the moving boundary.

An implicit Euler scheme is used to semi-discretize in pseudo-time equations (14) and (15) in the form

$$\frac{\hat{\mathbf{V}}^{v+1}-\hat{\mathbf{V}}^{v}}{\Delta\tau}+\hat{\mathbf{V}}^{v+1}+\beta\hat{\mathbf{G}}^{v+1}=\mathbf{E}^{n}, \tag{16}$$

$$\frac{\hat{p}^{v+1}-\hat{p}^{v}}{\Delta\tau}+\frac{1}{\delta}\nabla\cdot\hat{\mathbf{V}}^{v+1}=0, \tag{17}$$

with the initial values $\hat{\mathbf{V}}^{1}=\mathbf{V}^{n}$ and $\hat{p}^{1}=p^{n}$. After the solution has converged, $\mathbf{V}^{n+1}=\hat{\mathbf{V}}^{\kappa+1}$ and $p^{n+1}=\hat{p}^{\kappa+1}$, where $\kappa$ is the number of iterations for convergence.

Introducing $\Delta\mathbf{V}=\hat{\mathbf{V}}^{v+1}-\hat{\mathbf{V}}^{v}$ and similarly for $\Delta\mathbf{G}$ and $\Delta p$, Eqs. (16) and (17) can be recast in delta form

$$(1+\Delta\tau)\Delta\mathbf{V}+\beta\Delta\tau\Delta\mathbf{G}=\Delta\tau(\mathbf{E}^{n}-\hat{\mathbf{V}}^{v}-\beta\hat{\mathbf{G}}^{v}), \tag{18}$$

$$\Delta p+\frac{\Delta\tau}{\delta}\nabla\cdot(\Delta\mathbf{V})=-\frac{\Delta\tau}{\delta}\nabla\cdot\hat{\mathbf{V}}^{v}, \tag{19}$$

where $\Delta\mathbf{V}=[\Delta u,\Delta v,\Delta w]^{\mathrm{T}}$ and $\Delta\mathbf{G}(\mathbf{V},p)=[\Delta G_u,\Delta G_v,\Delta G_w]^{\mathrm{T}}$ with, for example, $\Delta G_u$ in cylindrical coordinates given by

$$\Delta G_u=\frac{\partial(\hat{u}^{v}\Delta u)}{\partial x}+\frac{1}{r}\frac{\partial(r\hat{v}^{v}\Delta u)}{\partial r}+\frac{1}{r}\frac{\partial(\hat{w}^{v}\Delta u)}{\partial\theta}+\frac{\partial(\Delta p)}{\partial x}-\frac{1}{\mathrm{Re}}\left[\frac{\partial^{2}(\Delta u)}{\partial x^{2}}+\frac{1}{r}\frac{\partial}{\partial r}\left(r\frac{\partial(\Delta u)}{\partial r}\right)+\frac{1}{r^{2}}\frac{\partial^{2}(\Delta u)}{\partial\theta^{2}}\right], \tag{20}$$

which is first-order accurate, consistent with the order of accuracy of the Euler pseudo-time semi-discretization discussed previously.

Eqs. (18) and (19) constitute an implicit system of equations, nonlinearly coupled by the term $\Delta\mathbf{G}$ and are written in global matrix form as

$$[\mathbf{I}+\beta\Delta\tau(\mathbf{M}_x+\mathbf{M}_r+\mathbf{M}_\theta)]\Delta\mathbf{f}=\Delta\tau\mathbf{S}, \tag{21}$$

in which $\mathbf{I}$ represents the unit matrix, the matrices $\mathbf{M}_x$, $\mathbf{M}_r$ and $\mathbf{M}_\theta$ contain the spatial derivatives with respect to $x$, $r$ and $\theta$ of the variable $\Delta\mathbf{f}=[\Delta u,\Delta v,\Delta w,\Delta p]^{\mathrm{T}}$. The vector $\mathbf{S}$ is given by

$$\mathbf{S}=\begin{bmatrix}\mathbf{E}^{n}-\hat{\mathbf{V}}^{v}-\beta\hat{\mathbf{G}}^{v}\\ -(1/\delta)\nabla\cdot\hat{\mathbf{V}}^{v}\end{bmatrix}. \tag{22}$$

Now, an approximate factorization [30] is applied to Eq. (21), thereby rewriting the implicit left-hand side as

$$[\mathbf{I}+\beta\Delta\tau(\mathbf{M}_x+\mathbf{M}_r+\mathbf{M}_\theta)]\Delta\mathbf{f}=(\mathbf{I}+\beta\Delta\tau\mathbf{D}_x)(\mathbf{I}+\beta\Delta\tau\mathbf{D}_r)(\mathbf{I}+\beta\Delta\tau\mathbf{D}_\theta)\Delta\mathbf{f}=\Delta\tau\mathbf{S}, \tag{23}$$

where $\Delta\mathbf{f}=[\Delta u,\Delta v,\Delta w,\Delta p]^{\mathrm{T}}$. The nonlinear term in Eq. (18) appears as $\Delta\mathbf{G}$. This term is linearized by simply lagging the velocity component.

An alternating direction implicit (ADI) scheme [31] is used in this analysis in order to separate the numerical integration of the linear system of Eq. (23). This is done by introducing the intermediate variables $\Delta\bar{\mathbf{f}}=[\Delta\bar{u},\Delta\bar{v},\Delta\bar{w},\Delta\bar{p}]^{\mathrm{T}}$ and $\Delta\tilde{\mathbf{f}}=[\Delta\tilde{u},\Delta\tilde{v},\Delta\tilde{w},\Delta\tilde{p}]^{\mathrm{T}}$, thereby leading to

$$(\mathbf{I}+\beta\Delta\tau\mathbf{M}_x)\Delta\tilde{\mathbf{f}}=\Delta\tau\mathbf{S}, \tag{24}$$

$$(\mathbf{I}+\beta\Delta\tau\mathbf{M}_r)\Delta\bar{\mathbf{f}}=\Delta\tilde{\mathbf{f}}, \tag{25}$$

$$(\mathbf{I}+\beta\Delta\tau\mathbf{M}_\theta)\Delta\mathbf{f}=\Delta\bar{\mathbf{f}}. \tag{26}$$

Thus, for each variable ($\Delta u$, $\Delta v$, $\Delta w$) and for each direction ($x$, $r$, $\theta$) the solution reduces to *tridiagonal systems of equations*. Since central differences are used to discretize the spatial differential operators, only the resulting tridiagonal systems of equations need to be solved, which is computationally efficient. In three-

dimensional (3-D) flow fields the matrix $\mathbf{M}_r$, for example, is

$$\mathbf{M}_r = \begin{bmatrix} \mathrm{M} & 0 & 0 & 0 \\ 0 & \mathrm{M} + 1/\beta + 1/(\mathrm{Re}\, r^2) & -\breve{w}^v/r & \partial/\partial r \\ 0 & 0 & \mathrm{M} + \breve{v}^v/r + 1/(\mathrm{Re} r^2) & 0 \\ 0 & (1/\beta\delta)(\partial/\partial r)(r) & 0 & 0 \end{bmatrix}, \tag{27}$$

where

$$M\varphi = \frac{\partial(r\breve{v}^v\varphi)}{r\,\partial r} - \frac{1}{\mathrm{Re}}\frac{\partial}{r\,\partial r}\left(r\frac{\partial\varphi}{\partial r}\right)$$

in which $\varphi$ is a dummy variable representing $v$ or $w$.

The implicit left-hand sides of the matrix equations (24)–(26) are then written in different $x$, $r$ and $\theta$ sweeps, in delta form and solved until $\Delta u$, $\Delta v$, $\Delta w$ and $\Delta p$ are obtained, and the values of $u$, $v$, $w$ and $p$ are calculated from

$$u^{n+1} = u^n + \Delta u, \quad v^{n+1} = v^n + \Delta v, \quad w^{n+1} = w^n + \Delta w, \quad p^{n+1} = p^n + \Delta p,$$

where $u^n$, $v^n$ and $w^n$ are the velocity components at the previous time level, $n$.

It should be mentioned that the values obtained for these quantities are the steady plus the complex unsteady components. To obtain the amplitude and phase angle with respect to the displacement of the outer cylinder, or real and imaginary parts of the velocity components and pressure, a Fourier Transform in discrete form is used [32], which reads

$$H(k) = \frac{1}{N}\sum_{n=0}^{N-1} g(n)\mathrm{e}^{-j\frac{2\pi kn}{N}}, \tag{28}$$

where $g(n)$ represents $u$, $v$, $w$, or $p$.

During the time-integration procedure, as far as the movement of the solid walls is concerned, on the inner cylinder the *non-dimensional displacement* $e_w(t)$ is zero, while on the outer cylinder in the plane of symmetry it is given by Eq. (13), with the velocity of the wall expressed by $\dot{e}_w(t) = \varepsilon\omega \sin \omega t$. The velocities of the boundary, $v_w$ and $w_w$, for the case of translational motion of the outer cylinder are given by Eq. (12); see Fig. 3(b). For translational motion the vertical displacement of the centre of the outer cylinder is given by $e_w(t)$; for rocking motion, the velocities $v_w$ and $w_w$ are linearly calculated with respect to the hinge position, Fig. 2, and they are

$$v_w = \dot{E}(t,x)\cos\theta, \quad w_w = -\dot{E}(t,x)\sin\theta, \tag{29}$$

where $\dot{E}(t,x) = \mathrm{d}E(t,x)/\mathrm{d}t$, and $E(t, x)$ is given by

$$E(t,x) = -\frac{e_w(t)}{l_2}x + \frac{e_w(t)(l_1+l_2)}{l_2}, \tag{30}$$

where $e_w(t)$ comes from Eq. (13), and $l_1$ and $l_2$ are constants, as shown in Fig. 2.

In this analysis, first the steady solution is obtained without any boundary motion and then the results of this solution are used to advance the unsteady solution, which is due to boundary movements. The major difference between the steady and unsteady solutions, besides the boundary movement, is the method of selecting the artificial compressibility factors, $\delta$, and pseudo-time steps, $\Delta\tau$. The selection of these factors for both steady and unsteady cases is done as in Chorin [29] and Soh [33].

In the first part of the present work, since the oscillation amplitude of the outer cylinder is assumed to be small, a fixed staggered grid [34], as shown in Fig. 4, related to the mean position of the moving boundary was used. Hyperbolic tangent and hyperbolic sine stretching functions [35] were used to obtain the best possible spatial resolution and concentrate more points in regions of higher velocity gradients, for example near solid walls and discontinuities.

The problems under consideration were solved for 2-D and 3-D configurations. In 2-D, i.e., for the $(r, \theta)$ flow problem, either the length of the cylinders is considered to be sufficiently long as compared to the radii for

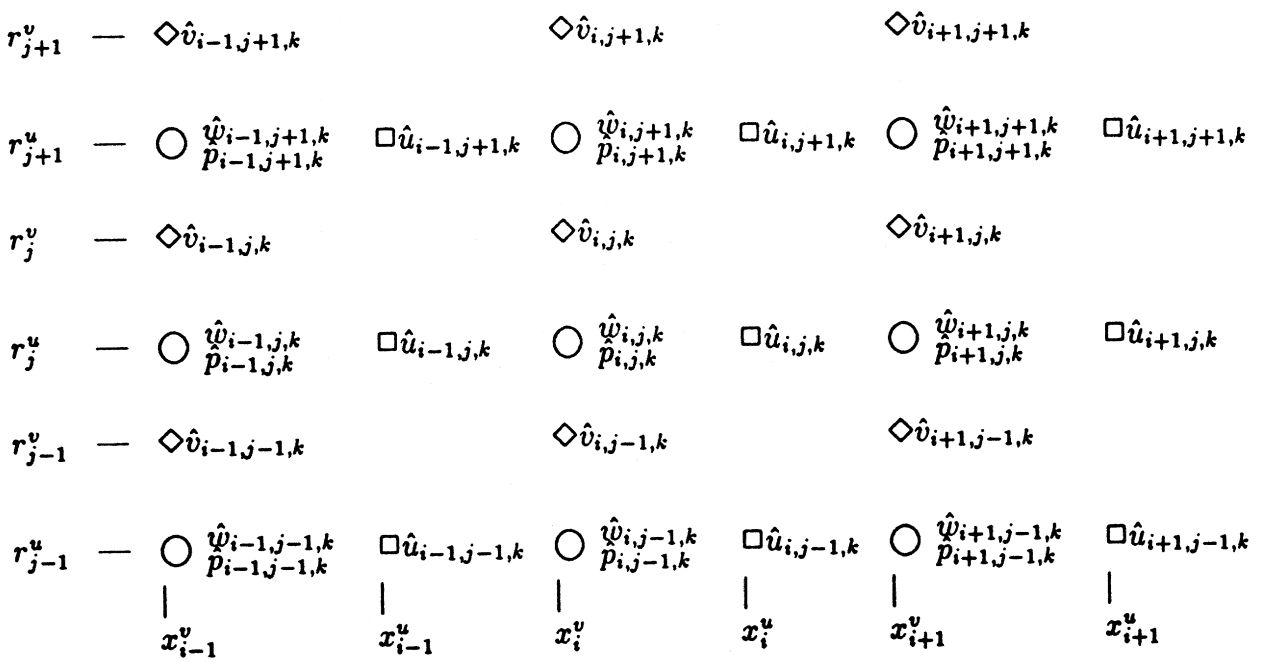


Fig. 4. Schematic representation of the staggered grid used in the spatial discretization of the three-dimensional nonlinear equations.

the $x$-component to be neglected in the computation, or the case of quiescent flow is considered. In 3-D annular flow problems, which are of major concern in this analysis, the initial direction of the flow is taken to be along the $x$-axis. Therefore, the initial values for the velocity and pressure should be defined at the inlet and outlet of the domain, as well as on the fixed and moving boundaries. The values for $u$, $v$ and $p$ are imposed at the inlet and outlet for the steady-state solution. The velocity profile in the steady state flow is given by the following non-dimensional equations:

$$u(r) = \frac{U^*(hr)}{U} = \frac{2[1-(r/r_i)^2 + (n^2-1)\ln(r/r_1)/\ln n]}{n^2+1-(n^2-1)/(\ln n)}, \quad v = 0, \quad w = 0, \tag{31}$$

where $U^*(hr)$ and $U$ are the dimensional axial and mean axial velocities in the annulus, respectively, and $n = r_o/r_i$. The velocities at the outlet of the annular space are obtained by extrapolating the known values of the flow variables from inside the domain. The pressure at the outlet is set equal to zero, and on the moving and fixed cylinders it is still set equal to zero due to the staggered girds used.

As mentioned earlier, this work is an improved version of the method used by Mateescu et al. [24–26] (solution of the full nonlinear versus the solution of the simple and linearized N–S equations developed by Mateescu and coworkers). Using this method, it was proved that (i) the method, which is characterized by a favourable velocity–pressure coupling, enhancing the stability and eliminating the need for added artificial damping terms, is stable up to large cell Reynolds number in laminar flows; (ii) this method is valid as applied to several flow problems, such as driven cavity flow, 2-D flow with a backward facing step and axisymmetric flow with backstep, for which the present method was found to be in good agreement with previous results [28,33,39,40], and (iii) the results obtained for the unsteady annular flow generated by small amplitude oscillations of the outer boundary of an annular conduit by using a three-point backward implicit time-discretization is free of spurious, numerically induced, oscillations of the pressure, which otherwise appeared when a Crank–Nicolson scheme is used instead. The method has also been validated experimentally by the authors of this work, in a paper to be published very soon.

### 2.2. Forces acting on the cylinder and structural equations of motion

The fluid dynamic forces, which are expressed in terms of inertial, damping and stiffness components are evaluated based on this viscous-flow analysis. The steady and unsteady forces are obtained by integrating the pressure and skin friction around the cylinder. The resultant forces acting on the structure per unit length, including the unsteady components, can be calculated by using the following stress equation in tensor form:

$$\mathbf{\Pi}_{ij} = -p\delta_{ij} + \mu\left(\frac{\partial u_i}{\partial x_j} + \frac{\partial u_j}{\partial x_i}\right), \tag{32}$$

where $\partial u_i/\partial x_j$ represents the partial derivative of the velocity component in the $i$ direction with respect to the $j$ coordinate, $\mu$ is the dynamic viscosity, and $\delta_{ij}$ denotes the Kronecker delta.

The steady forces, which are dependent on the gradients of the motion with respect to the axial direction, are derived from the longitudinal frictional force and from the pressurization of the flow to overcome the pressure drop. In this analysis, since these factors do not affect the problem, they are not considered.

The unsteady viscous forces arise from the normal and tangential friction forces containing the effect of the viscous pressure distribution along the circumference in a direction normal to the wall. Thus, the unsteady forces acting on the outer cylinder per unit length due to its oscillatory motion can be obtained by multiplying Eq. (32) by a unit vector normal to the outer cylinder and integrating the result:

$$F(t) = \int_0^{2\pi} \left(\tau_{rr}|_{r=r_o} \cos\,\theta - \tau_{r\theta}|_{r=r_o} \sin\theta\right) r_o\, \sin\,\theta\, \mathrm{d}\theta \tag{33}$$

in which $\tau_{rr} = \mathbf{\Pi}_{11}, \tau_{r\theta} = \mathbf{\Pi}_{12}$. The stress components can be written as

$$\tau_{rr}(r,\theta,t) = -p + 2\mu\frac{\partial v}{\partial r}, \quad \tau_{r\theta}(r,\theta,t) = \mu\left(\frac{1}{r}\frac{\partial v}{\partial \theta} + \frac{\partial w}{\partial r} - \frac{w}{r}\right). \tag{34}$$

The forces obtained from Eq. (33) are used in the equation of motion of the structure to analyze the dynamics and stability of the system. Hence, for translational motion of the outer cylinder one can write

$$M\ddot{y} + C\dot{y} + Ky = F(t), \tag{35}$$

where $M$, $C$, and $K$ are mass, damping and stiffness of the moving cylinder, respectively.

In the case of rocking motion, another stress component in the axial direction should be considered, i.e., $\tau_{rx} = \mu(\partial u/\partial r + \partial v/\partial x)$, and the force equation (33) is modified to

$$F(t) = \int_0^{2\pi} \left(\tau_{rr}|_{r=r_o} \cos\,\theta - \tau_{r\theta}|_{r=r_o} \sin\,\theta + \tau_{rx}|_{r=r_o} \frac{\mathrm{d}E(t,x)}{\mathrm{d}t}\right) r_o\, \sin\,\theta\, \mathrm{d}\theta, \tag{36}$$

where $\mathrm{d}E(t, x)/\mathrm{d}t$ is obtained from Eq. (30). The equation of motion of the cylinder about a hinge point (Fig. 2) is written as

$$J\ddot{\theta} + C_o\dot{\theta} + K_o\theta = M_o(t), \tag{37}$$

where $M_o(t)$ is the moment of the fluid forces about the fixed hinge point, $J$ is the moment of the inertia of the cylinder about the hinge axis and $\theta$ is the angular displacement of the cylinder; $C_o$ and $K_o$ are the rotational damping and stiffness constants of the cylinder.

Considering the characteristic length, $h$, and characteristic velocity, $U$, one can write Eq. (35) in dimensionless form as

$$\ddot{\varepsilon}(t) + 2\xi\omega_n\dot{\varepsilon}(t) + \omega_n^2\varepsilon(t) = \sigma\tilde{F}(\varepsilon,\dot{\varepsilon}), \tag{38}$$

where

$$\omega_n = \sqrt{\frac{K}{M}}\frac{h}{U} = \omega_n^*\frac{h}{U}, \quad \xi = \frac{C}{2\sqrt{KM}}, \quad \sigma = \frac{\rho^* h^3}{M}$$

and $\tilde{F}$ represents the non-dimensional fluid dynamic forces exerted on the cylinder. The equation of motion of the structure in rocking motion, Eq. (37), can similarly be written in non-dimensional form as

$$\ddot{\theta}(t) + 2\xi\omega_{nR}\dot{\theta}(t) + \omega_{nR}^2\theta(t) = \sigma\tilde{M}_o(\theta, \dot{\theta}), \tag{39}$$

where

$$\omega_{nR} = \sqrt{\frac{K_o h^2}{J}}\frac{h}{U} = \omega_{nR}^*\frac{h}{U}, \quad \xi = \frac{C_o h}{2\sqrt{K_o J}}, \quad \sigma = \frac{\rho^* h^5}{J},$$

with $\tilde{M}_o$ as the non-dimensional moment of the fluid dynamic forces exerted on the cylinder. In Eqs. (38) and (39), $\omega_n$ ($\omega_{nR}$ for rocking motion) and $\xi$ are the dimensionless frequency and damping ratio, respectively, while $\sigma$ is a dimensionless factor weighting the relative contribution of the fluid and mechanical forces; $\omega_n{}^*$ or $\omega_{nR}{}^*$ is the dimensional natural circular frequency of the structure, and $\rho^*$ is the dimensional fluid density. The non-dimensional fluid force $\tilde{F}$ is a function of $\varepsilon(t)$, $\dot{\varepsilon}(t)$, and $\ddot{\varepsilon}(t)$ through the added stiffness, added damping and added mass effects, respectively, but $\ddot{\varepsilon}(t)$ is not needed explicitly in the numerical evaluation of the fluid forces and $\varepsilon(t)$ is not needed either for the small amplitude analysis of the fluid forces. The non-dimensional fluid moment $\tilde{M}_o$ is, equivalently, a function of $\theta(t)$, $\dot{\theta}(t)$ and $\ddot{\theta}(t)$.

### 2.3. Solution of the structural equation and stability

To integrate Eq. (38) or Eq. (39), as the case may be, it is assumed at the beginning that the time level $t^n$ has been reached, where all the quantities necessary to describe the structural motion are known: the displacement $\varepsilon$, the velocity $\dot{\varepsilon}$, and the acceleration, $\ddot{\varepsilon}$, of the structure, and the fluid forces acting on it, $\tilde{F}(\varepsilon^n, \dot{\varepsilon}^n) \equiv \tilde{F}^n$. These quantities are known at all previous time levels $t^k$, $k \leqslant n$, and the solution is advanced to $t^{n+1}$. For structural motion analysis, this is done using a second-order Runge–Kutta scheme, defined by the sequence

*Predictor step*:

$$\varepsilon^{n+(1/2)} = \varepsilon^n + \frac{\Delta t}{2}\dot{\varepsilon}^n, \quad \dot{\varepsilon}^{n+(1/2)} = \dot{\varepsilon}^n + \frac{\Delta t}{2}\ddot{\varepsilon}^n, \tag{40,41}$$

$$\tilde{F}^{n+(1/2)} = \tilde{F}\left(\dot{\varepsilon}^{n+(1/2)}\right), \tag{42}$$

$$\ddot{\varepsilon}^{n+(1/2)} = -2\xi\omega_n\dot{\varepsilon}^{n+(1/2)} - \omega_n^2\varepsilon^{n+(1/2)} + \sigma\tilde{F}^{n+(1/2)}; \tag{43}$$

*Corrector step*:

$$\varepsilon^{n+1} = \varepsilon^n + \Delta t\dot{\varepsilon}^{n+(1/2)}, \quad \dot{\varepsilon}^{n+1} = \dot{\varepsilon}^n + \Delta t\ddot{\varepsilon}^{n+(1/2)}, \tag{44,45}$$

$$\tilde{F}^{n+1} = \tilde{F}(\dot{\varepsilon}^{n+1}), \tag{46}$$

$$\ddot{\varepsilon}^{n+1} = -2\xi\omega_n\dot{\varepsilon}^{n+1} - \omega_n^2\varepsilon^{n+1} + \sigma\tilde{F}^{n+1}, \tag{47}$$

thus, the displacement as well as velocity and acceleration of the outer cylinder as a function of time are determined.

One of the important factors influencing the stability analysis through the solution of, for example, Eq. (38) and similar ones, is the determination of the value of $\sigma$. Linearized potential flow theory provides the per unit length non-dimensional added mass, $\sigma_m$, for the geometry under consideration. This parameter may be expressed as

$$\sigma_m = \frac{\rho^* h^2}{m_a} = \frac{1}{\pi r_o^2}\frac{\zeta^2 - 1}{\zeta^2 + 1}; \tag{48}$$

where $m_a$ is the dimensional fluid added mass and $\zeta = r_o/r_i$. Thus, $\sigma M = \sigma_m m_a = \rho^* h^2$ or $\sigma_m/\sigma = M/m_a$ for 2-D analysis. To start the stability analysis, either this ratio must be known in advance, or it must be chosen in

such a way that a reasonable structural behaviour is obtained. When the fluid added mass exceeds the structural mass, numerical difficulties may arise (refer, for example, to Ref. [41]). In this analysis, only cases where the fluid-added mass is smaller than the mass of the structure, are considered. Thus, the value of $\sigma = \sigma_m/2.0$ chosen corresponds to a structural mass $M$ equal to twice the fluid added mass $m_a$ determined by potential flow theory.

In 3-D analysis, $\sigma M = \sigma_m m_a = \rho^* h^3$ and potential flow theory gives the equation of motion of the oscillating cylinder in translation as [20]

$$(1 + \sigma q_2)\ddot{\varepsilon} + (2\xi\omega_n + \sigma q_1)\dot{\varepsilon} + (\omega_n^2 + \sigma q_o)\varepsilon = 0, \tag{49}$$

where $q_2$, $q_1$ and $q_o$ are the non-dimensional added mass, added damping and added stiffness, given by

$$q_2 = \frac{M_a}{\rho^* h^3}, \quad q_1 = \frac{C_a h}{MU}, \quad q_o = \frac{K_a h^2}{MU^2}$$

in which $M_a$, $C_a$ and $K_a$ are similar dimensional quantities. Then, for 3-D potential flow, $\sigma$ is obtained from

$$\sigma q_2 = \frac{\rho^* h^3}{M}\frac{M_a}{\rho^* h^3} = \frac{M_a}{M}. \tag{50}$$

Once again, the mass ratio is selected to be $M/M_a = 2.0$, and to find $\sigma$ the added mass $q_2$ must be known. For this purpose the coupled structural and potential flow equations without the damping term are solved [36].

For rocking motion of the outer cylinder, a similar equation as Eq. (49) is solved but with $\varepsilon$ replaced by $\theta$. For this case, $\sigma q_2 = J_a/J$ applies and the ratio $J/J_a = 2.0$ is selected, as explained before.

For 3-D solution of axially variable annular configurations, the annular space considered consists of two concentric cylinders in which the inner one has a diffuser shape as shown in Fig. 1(c). In this figure, $hr_d$ is the diffuser height, which is equal to half the annular gap, e.g., $hr_d = hr_o - hr_i = h$. The diffuser half-angle was chosen to be either $\alpha = 6^\circ$ or $20^\circ$.

In order to generalize the problem, it is necessary to transform the annular space ($r^*$, $x^*$) in the physical domain of Fig. 1(c) into a rectangular computational domain ($r$, $x$). For this purpose, it is convenient to define the non-dimensional transformation equations as

$$r = \frac{Rhr - h^2 r_i \varepsilon(hx)}{R - h\varepsilon(hx)},$$
$$t = t^*, \quad \theta = \theta^*, \quad R = hr_i - hr_{id}, \quad X = hx_2 - hx_1, \tag{51}$$

where $h\varepsilon(hx) = Rh(x_2 - x)/X$; the starred quantities indicate the non-transformed physical quantities; $h\varepsilon(hx) = hr - hr_{id}$ indicates the radial distance from the centreline in Fig. 1(c) to any point on the surface of the diffuser section, and $hx_2 - hx_1$ is the axial length of this section. In this transformation, all functions having continuous partial derivatives in the physical cylindrical domain will be expressed in the form of functions in the computational domain and all conservation laws are satisfied. Although this transformation makes the matrix equation (27) more complex, it enhances the accuracy of the computation.

## 3. Time-dependent transformation analysis (large amplitude oscillation)

If the amplitude of the outer cylinder motion is considered to be small we can consider the boundary conditions to be applied at the *mean-position* (MP) of the outer cylinder, as in Section 2 and as shown in Fig. 3(a). For large amplitude motions, however, these boundary conditions are applied at the true position of the outer cylinder. The objective then is to solve the problem on a moving physical domain, i.e., for large amplitude oscillations. This necessitates the TDCT of the equations from the physical domain to a fixed computational counterpart. With the partial time derivatives in the physical solution equations replaced by partial time derivatives at fixed values of the curvilinear coordinates, the grid in the transformed plane is fixed even though the coordinate system in the physical plane is in motion. This introduces time derivatives of the coordinates into the transformed physical solution equations, in the role of additional convective terms; see, e.g., Ref. [37]. In this work, it is possible to perform all the computations on a fixed rectangular grid in the

transformed computational region *without any interpolation*, no matter how the grid points move in the physical domain as time progresses. The transformation procedure is briefly given here. For more details, see Mekanik [38].

It is necessary to transform the annular space $(r^*, \theta^*)$ from the more general problem of eccentric cylinders in the physical domain of Fig. 5(a) to the rectangular computational domain $(r, \theta)$, as shown in Fig. 5(b). This is achieved by the non-dimensional transformation equations

$$r = \frac{(r^* - R_i)}{[R_o^2 - \varepsilon^2(t^*)\sin\,\theta^*]^{1/2} - R_i + \varepsilon(\theta^*, t^*)},$$
$$\theta = \theta^*, \quad t = t^*, \tag{52}$$

where $\varepsilon(\theta^*, t^*) = \varepsilon(t^*)\cos\,\theta^*$, in which the starred quantities indicate the physical domain. The equivalent forms of Eqs. (5) and (6) in the transformed domain can be written in $(r, \theta)$ as

$$\frac{\partial \mathbf{V}}{\partial t} + rC\frac{\partial \mathbf{V}}{\partial r} + \mathbf{G}(\mathbf{V}, p) = \mathbf{0}, \tag{53}$$

$$\nabla \cdot \mathbf{V} = \frac{\partial u}{\partial x} + \frac{1}{r^*}\left[A\frac{\partial r^* v}{\partial r} + rB\frac{\partial w}{\partial r} + \frac{\partial w}{\partial \theta}\right] = 0. \tag{54}$$

The component $G_v(u, v, w, p)$ of vector $\mathbf{G}(\mathbf{V}, p)$, for example, is given by

$$\begin{aligned} G_v(u,v,w,p) = {} & \frac{\partial(uu)}{\partial x} + \frac{A}{r^*}\frac{\partial}{\partial r}(r^* vv) + \frac{1}{r^*}\frac{\partial(wv)}{\partial \theta} - \frac{w^2}{r^*} + A\frac{\partial p}{\partial r} + rC\frac{\partial v}{\partial r} + \frac{rB}{r^*}\frac{\partial(wv)}{\partial r} \\ & - \frac{1}{\mathrm{Re}}\left[\frac{\partial^2 u}{\partial x^2} + \frac{A}{r^*}\frac{\partial}{\partial r}\left(Ar^*\frac{\partial v}{\partial r}\right) + \frac{1}{r^{*2}}\frac{\partial^2 v}{\partial \theta^2} - \frac{2}{r^{*2}}\frac{\partial w}{\partial \theta} - \frac{v}{r^{*2}}\right. \\ & \left. + \frac{(rD + rB^2)}{r^{*2}}\frac{\partial v}{\partial r} + \frac{r^2B^2}{r^{*2}}\frac{\partial^2 v}{\partial r^2} - \frac{2rB}{r^{*2}}\frac{\partial w}{\partial r} + \frac{2rB}{r^{*2}}\frac{\partial^2 v}{\partial r\,\partial \theta}\right]. \end{aligned} \tag{55}$$

By this transformation, the matrices $\mathbf{M}_x$ and $\mathbf{M}_\theta$ remain intact, but $\mathbf{M}_r$ in Eq. (27) is changed and is now given by

$$\mathbf{M}_r = \begin{bmatrix} \mathrm{M} & 0 & 0 & 0 \\ 0 & \mathrm{M} + 1/\beta + 1/(\mathrm{Re}r^{*2}) & 2rB/(\mathrm{Re}r^{*2})\partial/\partial r - \breve{w}^v/r^* & A\partial/\partial r \\ 0 & -2rB/(\mathrm{Re}r^{*2})\partial/\partial r & \mathrm{M} + \breve{v}^v/r^* + 1/(\mathrm{Re}r^{*2}) & rB/(r^*)\partial/\partial r \\ 0 & (1/\beta\delta)(1/r^* + A\partial/\partial r) & rB/(\beta\delta r^*)\partial/\partial r & 0 \end{bmatrix} \tag{56}$$

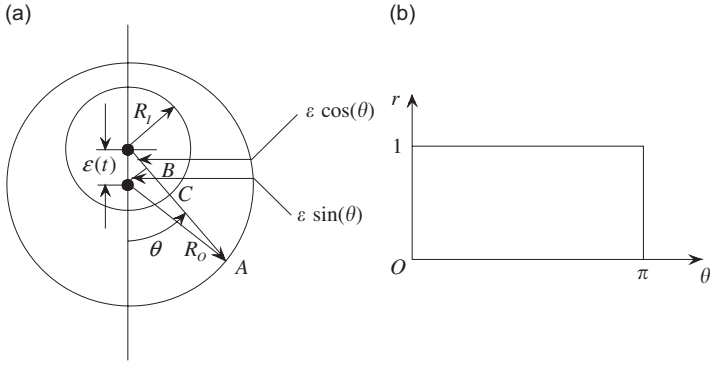


Fig. 5. (a) Physical and (b) transformed computational domains for two concentric cylinders with moving outer cylinder while in motion.

in which

$$\mathrm{M}\varphi = \left(rC - \frac{(rD + rB^2)}{\mathrm{Re}r^{*2}}\right)\frac{\partial\varphi}{\partial r} + \frac{A}{r^*}\frac{\partial(r^*\check{v}^v\varphi)}{\partial r} + \frac{rB}{r^*}\frac{\partial(\check{w}^v\varphi)}{\partial r} - \frac{1}{\mathrm{Re}}\left[\frac{A}{r^*}\frac{\partial}{\partial r}\left(Ar^*\frac{\partial\varphi}{\partial r}\right) + \frac{r^2B^2}{r^{*2}}\frac{\partial^2\varphi}{\partial r^2} + \frac{2rB}{r^{*2}}\frac{\partial^2\varphi}{\partial r\,\partial\theta}\right], \tag{57}$$

where $\varphi$ is a dummy variable representing $v$ or $w$ and $\check{v}^v$ and $\check{w}^v$ are the velocity components at pseudo-time level $v$.

In these equations, the transformation parameters are given by

$$A = \frac{1}{R(\theta,t) - R_i + \varepsilon(\theta,t)}, \quad B = \frac{A^2(r^* - R_i)(\varepsilon(t)\sin\theta)}{r}\left[\frac{-\varepsilon(t)\sin\theta\tan\theta}{R(\theta,t)} + 1\right],$$
$$C = -A\dot{\varepsilon}(t)\cos\theta\left[\frac{-\varepsilon(t)\sin\theta\tan\theta}{R(\theta,t)} + 1\right],$$
$$D = A^2\left\{[(F_1 + F_2)\varepsilon(t)\sin\theta + F_3\varepsilon(t)\cos\theta][\Phi(\theta,t)]^{1/2} - 2F_3F_4\varepsilon(t)\sin\theta\right\} \tag{58}$$

in which

$$R(\theta,t) = [R_o^2 - \varepsilon^2(t)\sin^2\theta]^{1/2}, \Phi(\theta,t) = R(\theta,t) - R_i + \varepsilon(\theta,t),$$
$$F_1 = -\varepsilon(t)[1 + (1/\cos^2\theta)](1/R(\theta,t))\sin\theta,$$
$$F_2 = -\varepsilon^3(t)(1/R(\theta,t)^3)\sin^3\theta,$$
$$F_3 = -\varepsilon(t)(1/R(\theta,t))\sin\theta\tan\theta + 1,$$
$$F_4 = -\varepsilon^2(t)[(1/R(\theta,t))\cos\theta - \varepsilon(t)]\sin\theta. \tag{59}$$

It is observed that the differential equations in the transformed domain become more complicated than in the physical one due to the extra convective and diffusive terms, in addition to the cross-derivative terms, which reflect the non-orthogonal nature of the coordinates, all of them arising from the transformation. During the solution procedure, the cross-derivative terms destroy the tridiagonal aspect of the system of equations to be solved; hence these terms are evaluated explicitly. From now on, the N–S and continuity equations (53) and (54) are solved on the fixed computational domain rather than on the moving physical domain. The rest of the procedure for solving the N–S equations and stability analysis is the same as for the MP analysis (in Section 2).

## 4. Results

This problem is the kind of problem that needs a complete parametric study. There are several factors influencing the response of the structure to fluid flow and affecting the final objective, i.e., the stability of the system. The non-dimensional parameters affecting the stability of the systems are: the gap width, $h$; the radii of the inner and outer cylinders, $r_i$ and $r_o$; the length of the central oscillating part of the outer cylinder, $l$; the fixed lengths upstream and downstream of the oscillating cylinder, $l_o$; the mean flow velocity, $U$; the Stokes number $S$ or equivalently the frequency of the oscillating cylinder, $\omega_n$; the amplitude of oscillation of the outer cylinder, $\varepsilon$; the mesh size; the compressibility factor, $\delta$; the pseudo-time step, $\Delta\tau$, and the real time step, $\Delta t$, to name but the most important factors. We cannot show the effects of all of these parameters on the stability of the system in a single paper, i.e., in the present work. Instead, we present samples of the results for certain sets of these parameters.[2]

A satisfactory grid generation and grid point distribution are the major requirements for the numerical solution to be accomplished successfully in terms of accuracy and stability. To this end, the numerical computations have been performed on a non-dimensional mesh with different axial lengths, different inner

[2]Certainly, a great deal remains to be done before the equivalent of stability maps, showing the effect of the main parameters, can be constructed, leading to design guidelines.

and outer radii for the annulus and $0 \leqslant \theta \leqslant \pi$, with $89 \times 12 \times 15$ grid points in the $x$, $r$, and $\theta$ directions, respectively. The effect of the number of grid points and of grid stretching in staggered mesh used on the accuracy of the numerical solution has already been studied extensively [38]. In 2-D analysis, there is about 0.2% difference between the results of the unsteady pressure amplitude for the mesh that consists of $12 \times 15$ grid points in the $r$- and $\theta$-directions *vis-à-vis* the meshes having $30 \times 15$ or $20 \times 30$ grid points in these directions. In 3-D solutions, the same conclusion is reached for the $x$-direction, i.e., a mesh size $65 \times 12 \times 15$ gives as accurate results as $89 \times 12 \times 15$ grid points in the $x$-, $r$- and $\theta$-direction. This is why in the present work the results for the latter grid distribution are presented, since it provides faster computation as well. Only representative results are presented. The figure captions describe the geometrical characteristics of the system analyzed.

For a quiescent fluid, in this analysis, in order to be able to obtain a solution, one needs to define an equivalent Reynolds number in the computational program. This can be done by selecting the Stokes number (based on the frequency of oscillation, $\omega^*$, annular gap width, $h$, and fluid viscosity, $\nu^*$), and using the relations $\mathrm{Re}_{D_h} = 2Uh/\nu^*$, $S = \omega^* h^2/\nu^*$ based on the hydraulic diameter of the annulus, from which the non-dimensional frequency $\omega$ can be written as $\omega = \omega^* h/U = 2S/\mathrm{Re}_{D_h}$. The computation can be done for different Reynolds and Stokes numbers (also defined as $S = \omega \mathrm{Re}_{D_h}/2$, which is related to the vibrational characteristics of the system) always in the laminar regime. For all of the results obtained in this work, the time step $\Delta t = T/N$ with $N = 19$ and the compressibility factor $\delta$ and pseudo-time step $\Delta\tau$ were chosen based on the criteria supplied by Soh and Goodrich [28] and Chorin [29]. Also, numerical experiments have been performed to determine the optimum values for the artificial compressibility and the pseudo-time step in order to achieve rapid convergence. It was found that these numerical experimentations confirmed the following theoretical relations derived earlier by Mateescu et al. [27], based on the theory of characteristics: $\delta = 1/(4q^2\Delta t)$ and $\Delta\tau = C\Delta x/[\beta q + (\beta^2 q^2 + \beta/q)^{1/2}]$, where $q = \sqrt{u^2 + v^2 + w^2}$, $\beta = 2\Delta t/3$ and $C$ is the Courant–Friedrichs–Levy number, for which an average value between 30 and 40 has been considered. These conclusions have been used in the present analysis to define the stretched staggered mesh used for various problems and to determine the optimum values for $\delta$ and $\Delta\tau$ as functions of the non-dimensional real-time step, $\Delta t$. Numerical computations were also performed to study the effect of the non-dimensional real-time step, $\Delta t$, on the accuracy and convergence of the present numerical solution [38]. Typical results showing the effect of $\Delta t = T/N = 2\pi/N$ on the present 3-D numerical solution for the reduced unsteady pressure amplitude at $x = l/2$, $r = 9.965$ and $\theta = 7.5^\circ$ for $r_i = 9$, $r_o = 10$, $l = 100$, $l_0 = 100$, $\mathrm{Re}_{D_h} = 250$, $S = 25$ and $\varepsilon = 0.1$ show that accurate solutions are obtained with a number $N$ of real-time steps per oscillatory cycle between 40 and 60, and that $N = 30$ can still be used with a reasonably good accuracy for 3-D problems, and $N = 19$ for 2-D flows. However, although the number of pseudo-time iterations decreases with increasing $N$ (it is halved when $N$ is increased from 19 to 40), the overall computations become expensive for larger numbers of real-time steps per oscillatory cycle. For this reason, most of the results given in this paper were computed with $N = 19$, which still provide an acceptable engineering accuracy. In all computations, convergence was reached and the iterations were stopped in pseudo-time when the rms values of the numerical residuals of the momentum and continuity equations were all less than $10^{-4}$, which is low enough to ensure that the governing equations of fluid motion are satisfied for each real-time step. Also, the validation of the present results with the results of references [24–26] based on the same method of solution (MP analysis) indicates that this value for the residuals is small enough to ensure the accuracy of the results obtained in this work.

The order of the presentation of the results is: first for uniform annular geometry, then for a non-uniform annulus with a backward facing step, and finally for a diffuser-shaped geometry. Section 4.1 presents the MP results, while Section 4.2 presents the TDCT results.

### 4.1. Mean position analysis results

#### 4.1.1. Results for prescribed oscillatory motion

Figs. 6(a) and (b) illustrate the unsteady pressure and phase angle for different amplitudes of oscillation of the outer cylinder with translational motion in a uniform annular geometry. It can be seen that the amplitude of the pressure increases almost linearly with the amplitude of oscillation. The phase angle also increases with

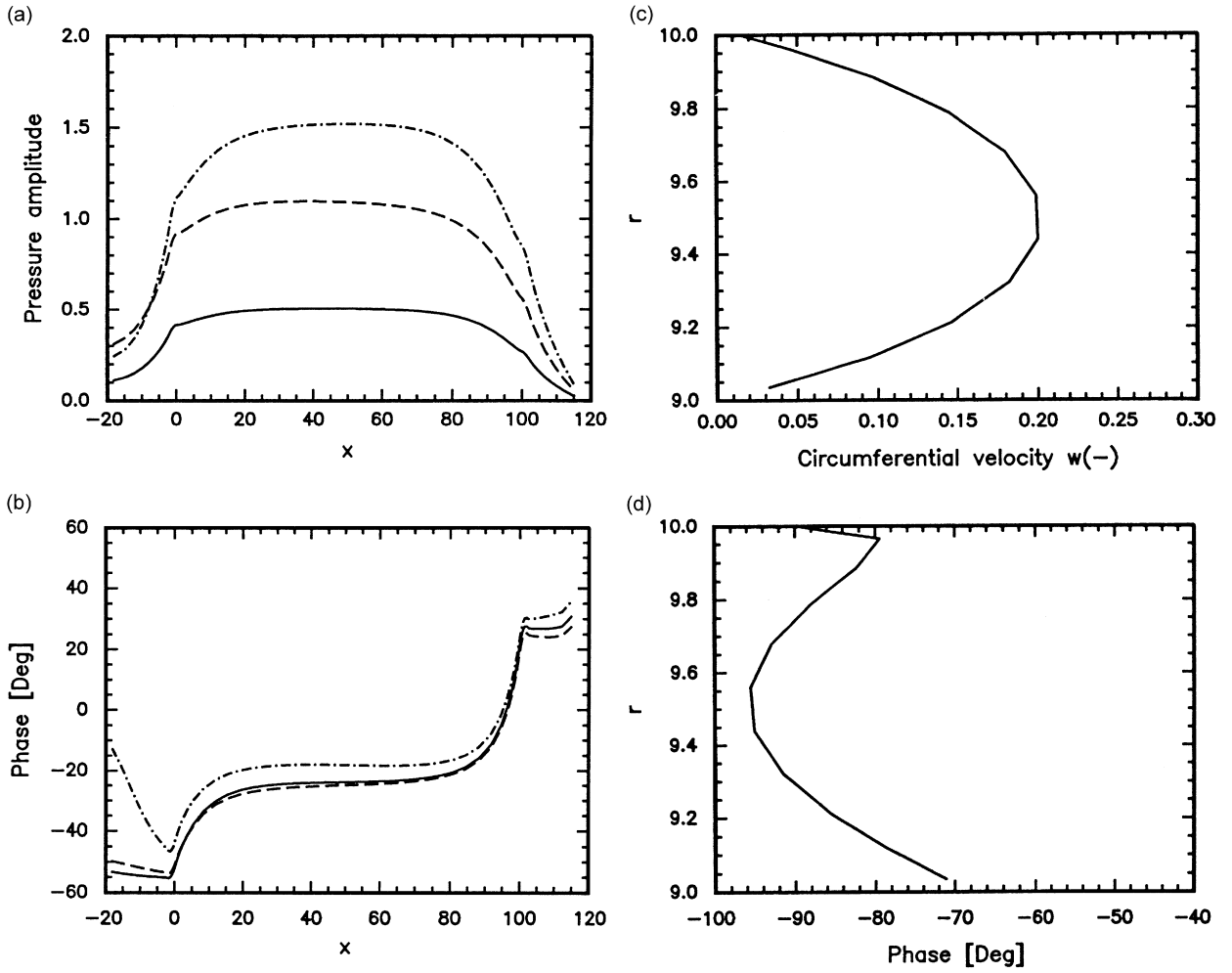


Fig. 6. Left: (a) The non-dimensional unsteady pressure $p$ and (b) the corresponding phase with respect to the translational displacement of the outer cylinder versus axial coordinate of the cylinder in a uniform annular geometry at $r = 9.965$, $\theta = 7.5°$; ——, $\varepsilon = 0.1$; - - - -, $\varepsilon = 0.2$, – · – · –, $\varepsilon = 0.3$. Right: (c) the distribution of the circumferential velocity $w$ versus $r$ and (d) the corresponding phase; for $\varepsilon = 0.1$, $X = 50$, $\theta = 45°$. In both left and right figures $\mathrm{Re}_{D_h} = 250$, $r_i = 9$, $r_o = 10$, and $\omega = 0.2$.

amplitude. Figs. 6(c) and (d) present the circumferential velocity $w$ as a function of the radial coordinate $r$, and the corresponding phase angle obtained at $X = 50$ and $\theta = 45°$. In the notation of the figure, the moving part of the outer cylinder extends from $X = 0$ to 100. It is noted that both the amplitude and phase are sensibly constant over the central portion of the moving cylinder, i.e., $20 < X < 80$ approximately. It should also be noted that both the amplitude and the phase are dependent on the frequency of oscillation $\omega$—as well as on the other system parameters.

Figs. 7(a) and (b) present the pressure and phase angle for different amplitudes of oscillation of the outer cylinder with translational motion of the outer cylinder for annular geometry with a backstep. Again, the pressure amplitude is a function of oscillation amplitude. The phase angles remain almost the same. Figs. 7(c) and (d) show the circumferential velocity $w$ and its phase angle obtained at $X = 20$ and $\theta = 45°$, which is just after the step. In terms of the form of $w(r)$, it is remarkable that it is only slightly skewed, in the sense that the maximum is only slightly closer to the inner boundary (the centre-body) than to the outer cylinder wall. It is immediately obvious that the shape of both pressure and phase in Figs. 7(a) and (b) are quite different from those in Fig. 6(a) and (b). Clearly, the expansion in the annular passage at $X = 20$ has an effect throughout the annulus, from $X = -20$ to 60 (though only the results from $X = 0$ up to 40 are required).

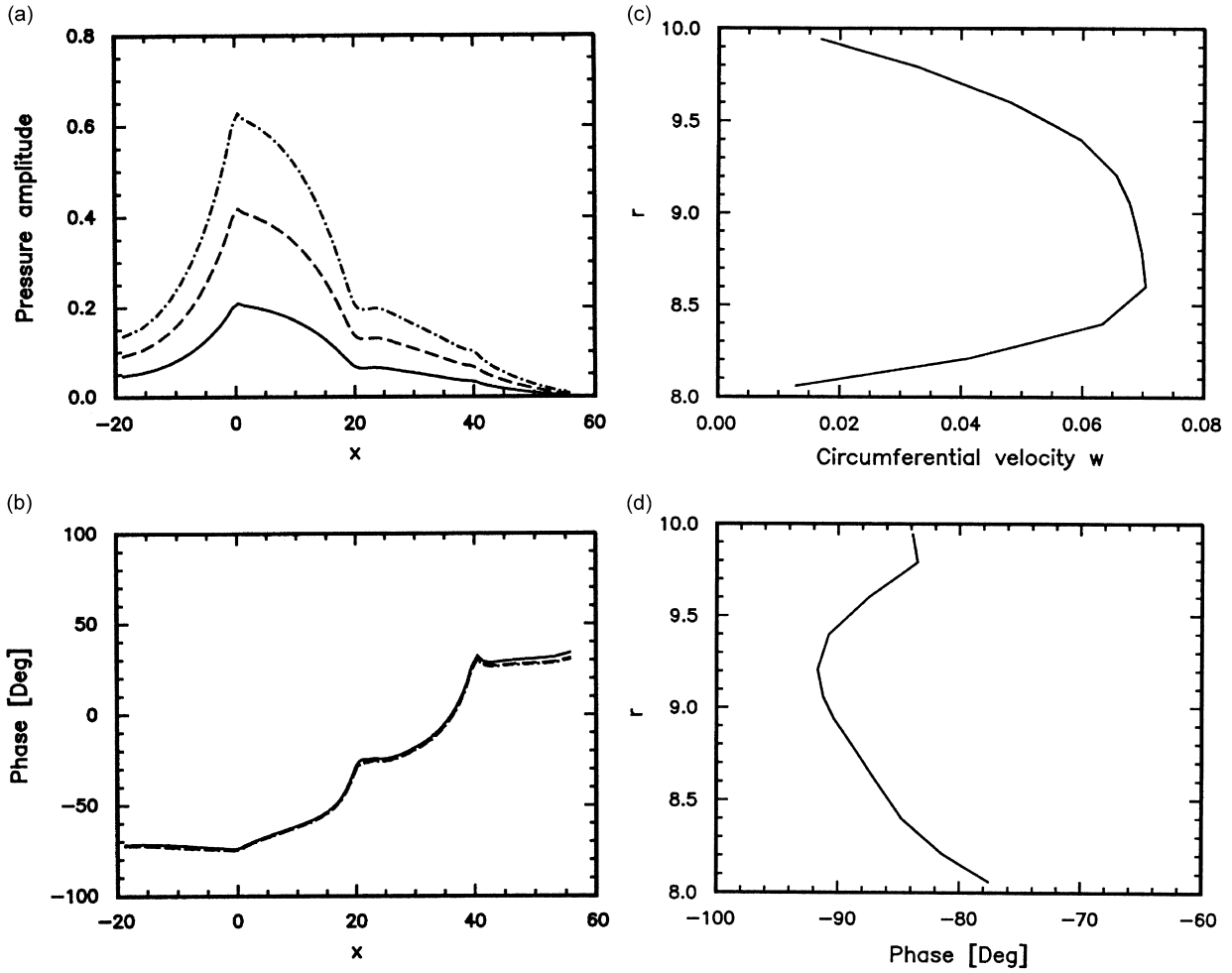


Fig. 7. Left: (a) The non-dimensional unsteady pressure $p$ and (b) the corresponding phase with respect to the translational displacement of the outer cylinder versus axial coordinate of the cylinder in uniform annular geometry with a backstep at $r = 9.965$, $\theta = 7.5°$; ——, $\varepsilon = 0.1$; ----, $\varepsilon = 0.2$, – · – · –, $\varepsilon = 0.3$. Right: (c) the distribution of the non-dimensional circumferential velocity $w$ versus $r$ and (d) the corresponding phase; for $\varepsilon = 0.1$, $X = 20$, $\theta = 45°$. In both left and right figures $\mathrm{Re}_{D_h} = 250$, $r_{id} = 8$, $r_i = 9$, $r_o = 10$ (Fig. 1(b)), and $\omega = 0.2$.

Significantly, the largest pressure amplitude in this case, near $X = 0$, is significantly lower ($p \approx 0.6$) than for the uniform annulus ($p \approx 1.5$ in Fig. 6(a)). Hence, the effect of the enlargement propagates all the way to the upstream end.

Figs. 8(a) and (b) present the unsteady pressure and phase angle for different amplitudes of oscillation of the outer cylinder with rocking motion in the uniform annular geometry. The hinge about which the rocking motion takes place is located at $X = 81.0$. Figs. 8(c) and (d) present the unsteady pressure and phase angle for backstep geometry when the outer cylinder is in rocking motion.[3] Here, the hinge is located at $X = 82.0$. When there is a fluid flow, the effects of having a step are clearly seen in this figure. Figs. 8(a) and (b) are not directly comparable in terms of magnitudes with Figs. 6 and 7 since the system parameters are very different (higher Re and $\omega$, and smaller $\varepsilon$). However, some qualitative differences in the results for rocking motion between this figure and Fig. 7 are to be noted. For a uniform annulus, the highest amplitude occurs at the upstream end (where the oscillation amplitude is largest, as the hinge is towards the downstream end of the rocking

[3]What has been shown in Fig. 8(d) is what was obtained by FFT analysis of the results. In Fig. 8(d), since $\tan 200° = \tan(-160°)$, the jump in the region $85 < x < 95$ of this figure can be removed and a smooth curve can be drawn at $\varphi = -160°$.

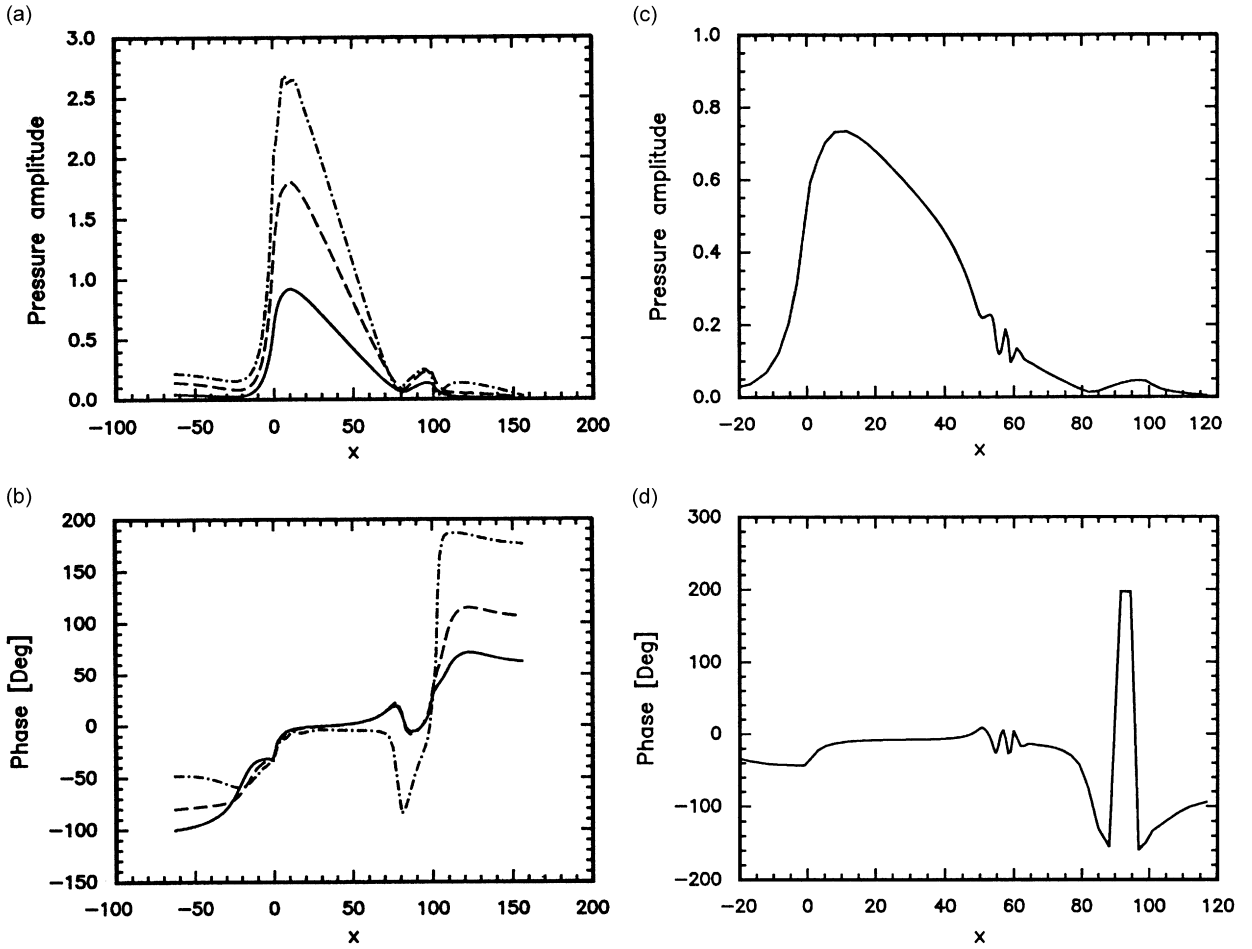


Fig. 8. (a, c) The non-dimensional unsteady pressure amplitude and (b, d) phase angle during rocking motion of the outer cylinder for $r_i = 4.785$, $r_o = 5.785$. Left figures for uniform annular space with $\omega = 0.703$, $\mathrm{Re}_{D_h} = 2900$, ——, $\varepsilon = 0.05735$; - - - -, $\varepsilon = 0.1075$; – · – · –, $\varepsilon = 0.16125$ and hinge location at $X = 81.0$. Right figures are for a backstep geometry, for $\omega = 0.5$, $\mathrm{Re}_{D_h} = 400$, $\varepsilon = 0.1075$ and hinge location at $X = 82.0$.

cylinder); also of importance is the fact that the largest amplitude attained is much larger than in Fig. 7 (or, for that matter, in Fig. 6), as a result of the flow velocity and also $\omega$ being so much higher in this case. It is also remarkable that the pressure distributions for the uniform geometry (Fig. 8(a)) and backstep geometry (Fig. 8(c)) in this case are much more similar to each other than those in Figs. 6 and 7 are.

Figs. 9(a) and (b) present the unsteady pressure and phase angle for different oscillation amplitudes of the outer cylinder in translational motion for annular flow in a diffuser-shape geometry with $\alpha = 6^\circ$. This figure should be compared with the results of Figs. 7(a) and (b). In the downstream portion of the annulus, in Fig. 9(a), the pressure recovery is noticeable *vis-à-vis* the backstep geometry in Fig. 7(a). The phase angles are also almost independent of the vibration amplitudes. The unsteady pressure and phase angles shown in Fig. 9(c) and (d) have been obtained for a diffuser angle $\alpha = 20^\circ$. These results indicate that the behaviour of this kind of diffuser is similar to that of a system with a backstep geometry, and that the pressure recovery is not as pronounced as in the case of a diffuser with $\alpha = 6^\circ$.

A comparison between the unsteady pressure and phase angle for three different geometries is made in Fig. 10. This figure shows that the pressure recovery is more pronounced for a diffuser with $\alpha = 6^\circ$ than for either the diffuser with $\alpha = 20^\circ$ or the backstep geometry. The phase angle results for the three geometries also display different trends, and clearly this has repercussions on the stability of such systems.

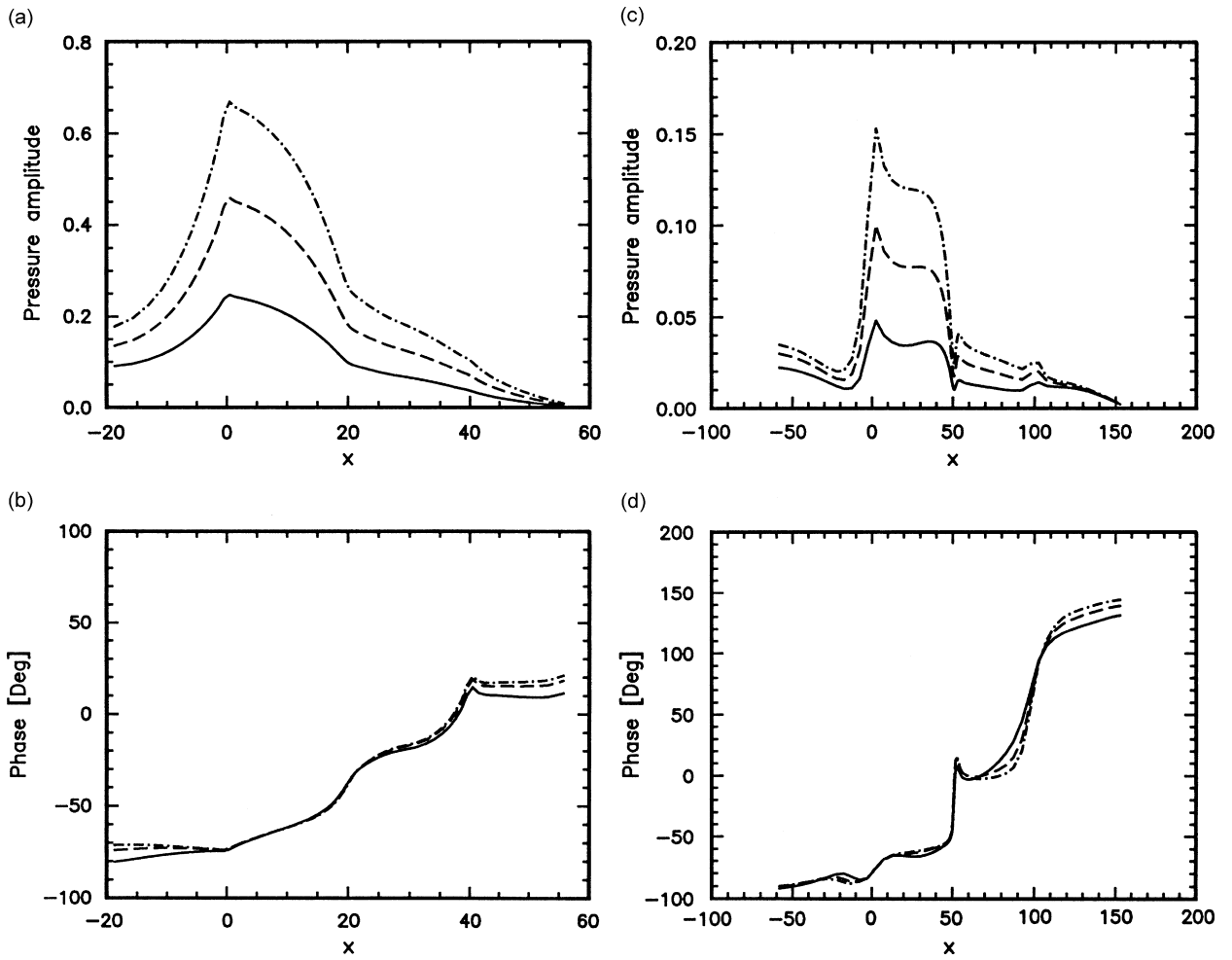


Fig. 9. (a, c) The non-dimensional unsteady pressure and (b, d) phase angle versus axial length of the cylinder in translational motion for $\mathrm{Re}_{D_h} = 100$, $\omega = 0.1$, ——, $\varepsilon = 0.05735$; ----, $\varepsilon = 0.1075$ and – · – · –, $\varepsilon = 0.16125$. Left figures for $\alpha = 6^\circ$, $r_{id} = 8$, $r_i = 9$, $r_o = 10$, $l = 40$ (Fig. 1(c)) at $r = 9.942$. Right figures for $\alpha = 20^\circ$, $r_{id} = 3.785$, $r_o = 5.785$, $l = 100$ at $r = 5.727$.

### 4.1.2. *Stability of the system*

For stability analysis, we assume that the length of the structure is very large; hence for simplicity, we can use the method of solution of Section 2 in two dimensions $r$ and $\theta$ and eliminate the calculation in the $x$ direction. To study the added damping produced by the motion of the cylinder in the fluid, the coefficient of the structural damping, $C$ appearing in Eq. (35), is taken to be zero. Fig. 11 shows the displacement of the oscillating cylinder as a function of Reynolds number, for a system with $r_i = 9$ and $r_o = 10$. From Fig. 11, we see that at very low Reynolds number, $\mathrm{Re}_{D_h} = 4$, viscosity dominates the solution and motion is so highly damped that no oscillations are possible: the system is overdamped. As the Reynolds number increases, $\mathrm{Re}_{D_h} = 200$, damped oscillation develops. As the Reynolds number becomes larger, $\mathrm{Re}_{D_h} = 2000$, the viscous solution gets closer to the potential (inviscid) flow solution (also shown in the figure), i.e., zero dissipation, and hence zero fluid damping [20].

For an annular geometry of given dimensions and outer cylinder of mass $M$, the change in natural frequency $\omega_n$ (of the system in vacuum) corresponds to a system in which the spring stiffness $K$ is varied. The selection of natural frequency $\omega_n = 1$ indicates that, for a stiff system, the viscous solution is not as highly damped as for a system which has less rigidity, i.e., $\omega_n = 0.1$. Fig. 12 shows the effect of different values of $\omega_n$ on the stability of the structure in a uniform annular geometry when the outer cylinder is in

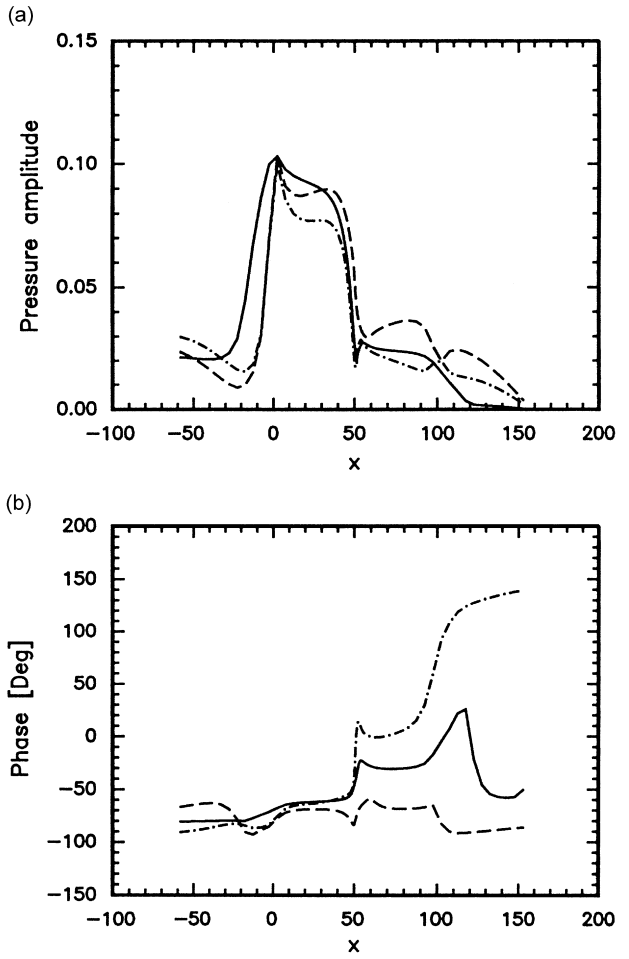


Fig. 10. (a) The non-dimensional unsteady pressure and (b) phase angle for $\mathrm{Re}_{D_h} = 100$, $\omega = 0.1$, $r_{id} = 3.785$, $r_o = 5.785$, $\varepsilon = 0.1075$ at $r = 5.727$, $\theta = 7.5^\circ$. Comparison between the results obtained for: ——, backstep; – – – –, diffuser with $\alpha = 6^\circ$; – · – · –, diffuser with $\alpha = 20^\circ$.

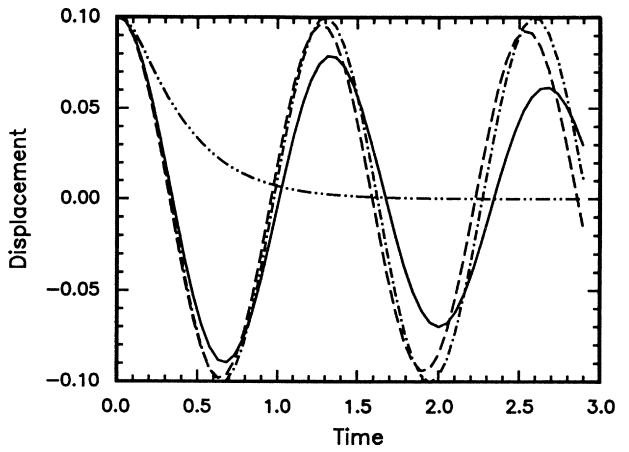


Fig. 11. Displacement, $\varepsilon$, of the outer cylinder in translational motion versus time, $T_n = 2\pi/\omega_n$, with $\omega_n = 1$ for a 2-D annulus; – · · – · · –, $\mathrm{Re}_{D_h} = 4$; ——, $\mathrm{Re}_{D_h} = 200$; – – – –, $\mathrm{Re}_{D_h} = 2000$; – · – · –, potential flow [20].

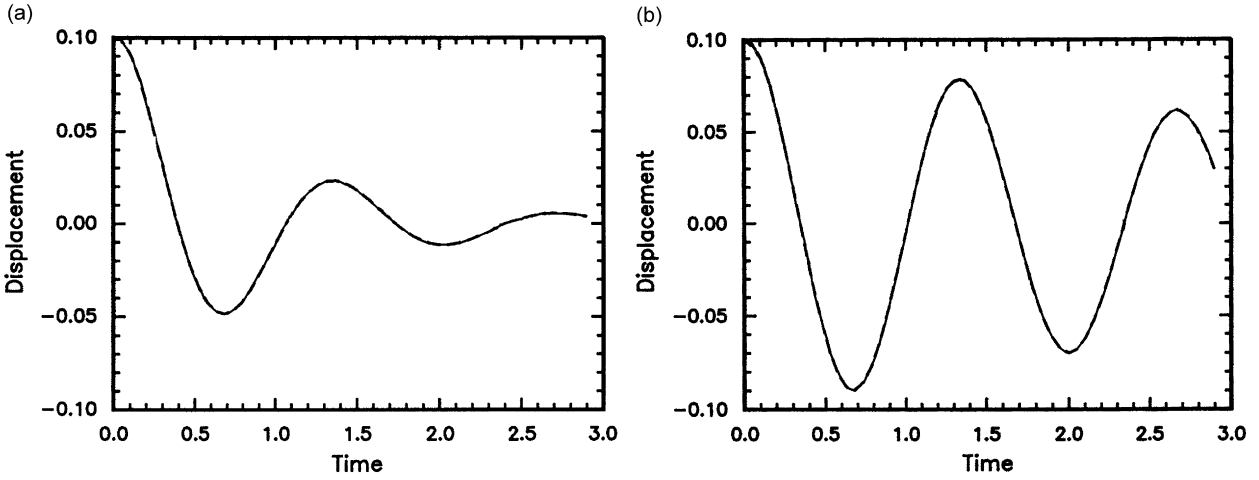


Fig. 12. Displacement, $\varepsilon$, of the outer cylinder in translational motion versus time, $T_n = 2\pi/\omega_n$, for $\mathrm{Re}_{D_h} = 200$ and uniform annular flow: (a) $\omega_n = 0.1$, (b) $\omega_n = 1$.

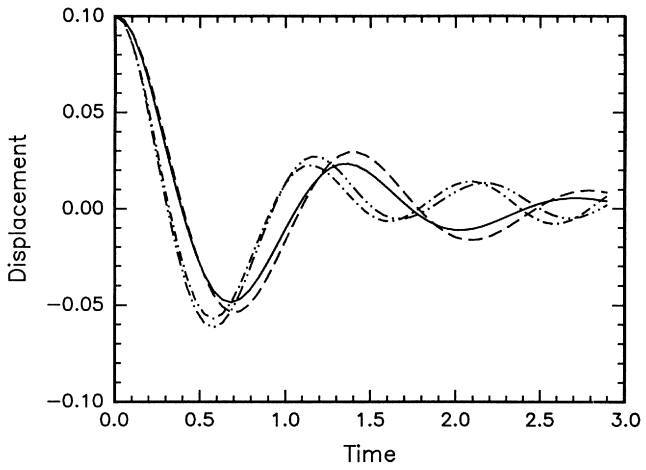


Fig. 13. Comparison between the dynamical behavior of the system in translational motion for different geometries and for $\omega_n = 0.1$ and $\mathrm{Re}_{D_h} = 200$; ——, uniform; – – – –, backstep; – · – · –, diffuser with $\alpha = 6°$; – · · – · · –, diffuser with $\alpha = 20°$.

translational motion. Clearly, for the stiffer system ($\omega_n = 1$) the damping is less pronounced, and the effective logarithmic decrement is much smaller. Figs. 13–16 present the time evolution for the displacement of the vibrating outer cylinder, where the viscous flow results were obtained for a less stiff structure ($\omega_n = 0.1$).

Fig. 13 presents a comparison of the dynamical behaviour of all the annular geometries considered for translational motion and $\omega_n = 0.1$, $\mathrm{Re}_{D_h} = 200$. It is seen that the most stable (most highly damped) system is the uniform annular system and the least stable is that involving a backstep. Also, regarding the coupled frequency of oscillation it is clear that the oscillation frequency changes with the geometry, i.e., the smaller coupled oscillation frequency belongs to the backstep geometry while the larger one belongs to the diffuser geometry with half-angle $\alpha = 6°$.

Finally, Fig. 14 shows the results of a system with uniform annular geometry in rocking motion, for a slightly higher Re than in the foregoing and structural damping $C_o$ (Eq. (37)) equal to zero. This figure indicates that the system initially appears to diverge, but it recovers and then oscillates with almost constant frequency and amplitude; i.e., it approaches a flutter-related limit-cycle oscillation.

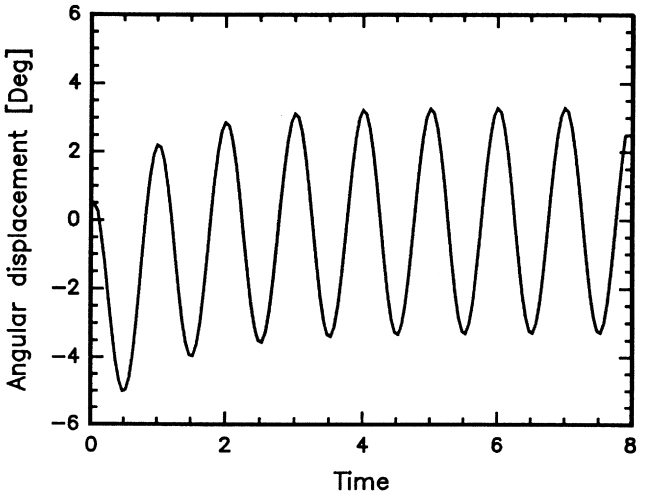


Fig. 14. Displacement $\theta$ versus time, $T_n = 2\pi/\omega_n$, for $\omega_n = 0.1$, $\mathrm{Re}_{D_h} = 250$. Uniform annular geometry with rocking motion of the outer cylinder, hinge point at $X = 90.0$.

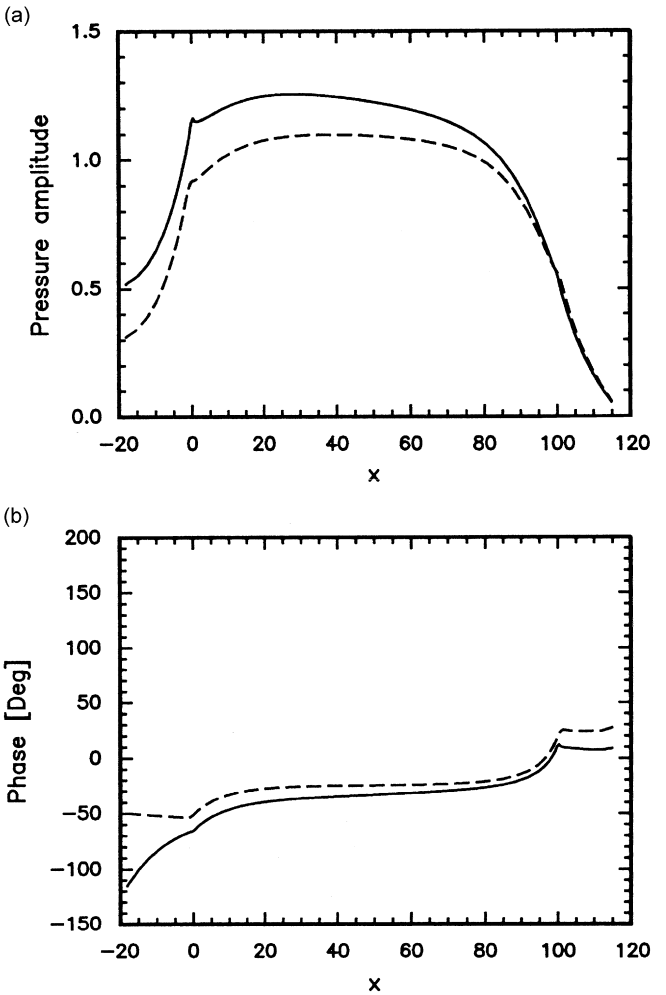


Fig. 15. (a) The non-dimensional unsteady pressure and (b) phase angle for $\mathrm{Re}_{D_h} = 250$, $\omega = 0.2$, $r_i = 9.0$, $r_o = 10.0$, $\varepsilon = 0.2$ at $r = 9.965$, $\theta = 7.5^\circ$; ——, time-dependent transformation analysis; – – – –, mean-position analysis.

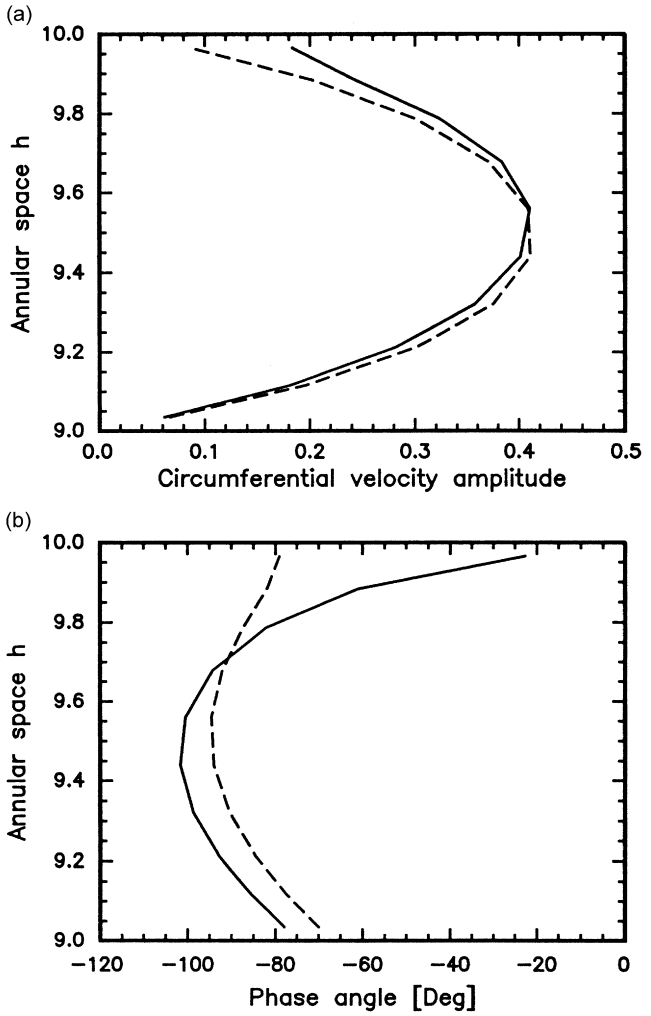


Fig. 16. (a) The non-dimensional circumferential velocity $w$ and (b) phase angle with respect to the displacement of the outer cylinder for $\mathrm{Re}_{D_h} = 250$, $\omega = 0.2$, $r_i = 9.0$, $r_o = 10.0$, $\varepsilon = 0.2$ at mid-gap, $X = 50$ and $\theta = 45^\circ$; ——, time-dependent transformation analysis; – – – –, mean-position analysis.

### 4.2. Time-dependent transformation analysis results

The computations with the model for larger amplitude oscillations using the TDCT were performed for the same annular spaces, the same meshes, etc. as those for small amplitude oscillations using the MP model, for the purpose of comparison of the results. As a first step, the amplitude and velocity of the moving boundary are calculated using the appropriate equations and are kept constant throughout the pseudo-time relaxation. The other initial and boundary conditions are given or calculated following the same procedure as described in the previous sections.

Fig. 15 presents the unsteady pressure amplitude and phase angle versus the axial length of the cylinder for both MP and TDCT analyses; in this figure $l_o = 20$, $r_i = 9.0$, and $r_o = 10.0$ as in Fig. 1(a). This result shows a 25% and 16% increase, approximately, in the pressure amplitude and phase, respectively, when the more accurate TDCT analysis is used.

Fig. 16 demonstrates the effect of larger-amplitude oscillation on the circumferential velocity $w$ and on its phase angle. It is seen that the amplitude of $w$ does not vary too much, but a substantial change in its phase angle is noted. It must be mentioned that in Fig. 16 the annular space $h$ shown is $0 \leqslant h \leqslant 1$, whereas it is

$9 \leqslant h \leqslant 10$ in the MP analysis; this relation is simple and obvious if one notes that the non-dimensional annular gap is always $h = 1$, and hence one can present the results for both methods on the same diagram.

Fig. 17 is presented to demonstrate the effects of the change in annular dimensions, $r_i = 4.785$ and $r_o = 5.785$ as compared to those in Fig. 15 (see Fig. 1(a)), and also the change in the lengths of the fixed upstream and downstream portions of the outer cylinder, $l_o = 60$, on the results. In Fig. 17(a) and (b), the comparison between the results obtained using both methods of solution but for higher frequency of oscillation ($f = 20$ Hz) in quiescent fluid is demonstrated. In Fig. 17(a) compared to Fig. 15(a), although the fixed portions at the extremities of the moving cylinder have larger lengths, $l_o = 60$ in Fig. 1(a), the time-dependent solution demonstrates an increase of 6% in the pressure amplitude, which is due to the larger value of the oscillation frequency. Fig. 17(b) presents, as usual, lower values for the phase angle, as compared to the one obtained by the MP analysis. Figs. 17(c) and (d) present the pressure amplitude and phase angle for fluid flow with $\mathrm{Re}_{D_h} = 2900$ and frequency of oscillation $f = 20$ Hz. Once again, the mean values for the unsteady pressure obtained from the two approaches are almost the same since the amplitude of oscillation in this case is small, i.e., $\varepsilon = 0.05375$; the effect on the phase angle is similar to that in previous figures.

Similar results for the backstep geometry are shown in Fig. 18. As expected, there are some differences in the results; i.e., there is an overall increase in the value of pressure in comparison to that obtained through the MP analysis; also, the phase angle (after the step geometry) is closer to zero than the corresponding value obtained

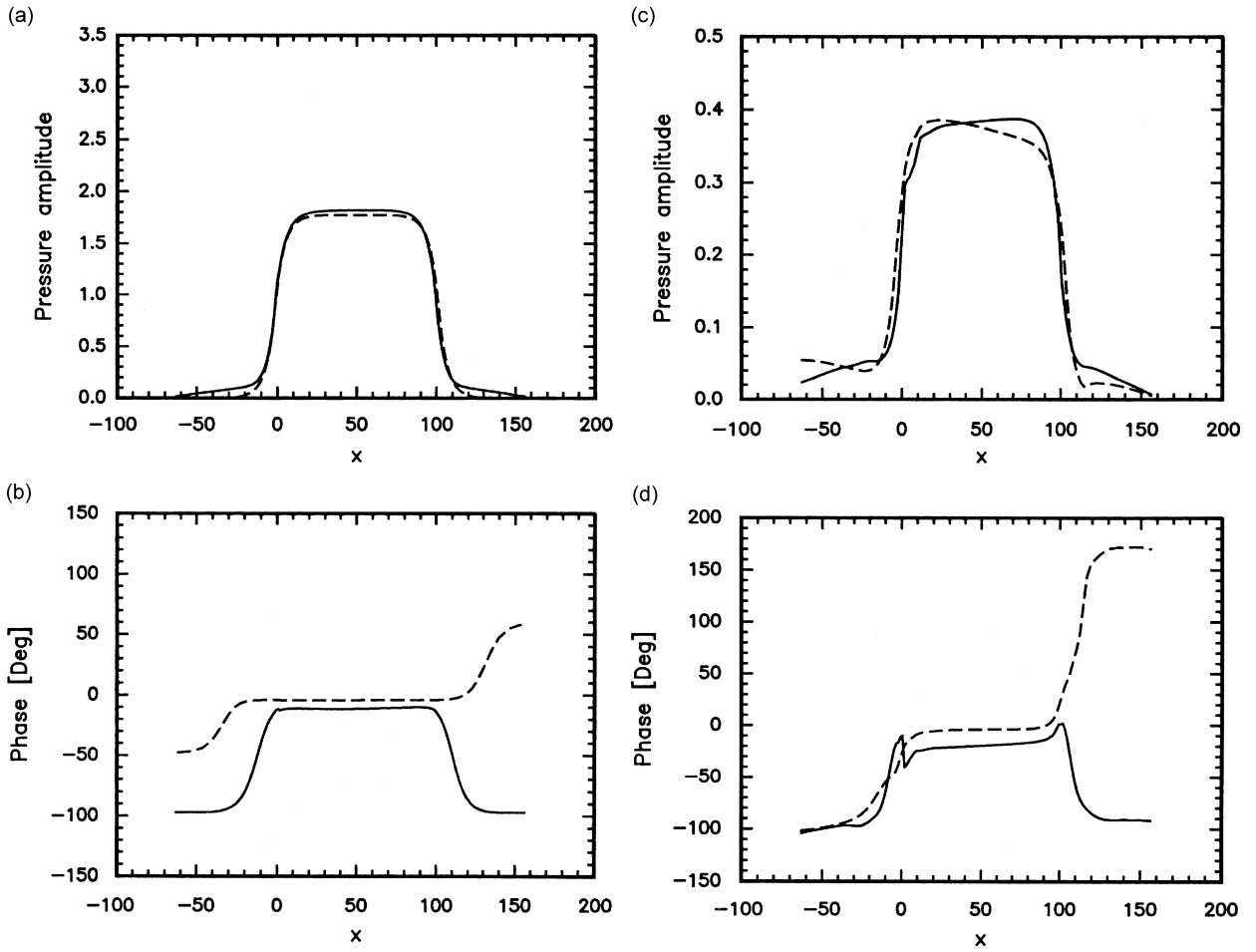


Fig. 17. (a, c) The non-dimensional unsteady pressure and (b, d) phase angle for $r_i = 4.785$, $r_o = 5.785$, $\varepsilon = 0.05375$ at $r = 5.727$, $\theta = 7.5°$; ——, time-dependent coordinate transformation analysis; – – – –, mean position analysis. Figures (a, b) for $U = 0.0$, $\omega = 1$ ($f = 20$ Hz) and Figs. (c, d) for $\mathrm{Re}_{D_h} = 2900$, $\omega = 0.463$ ($f = 20$ Hz).

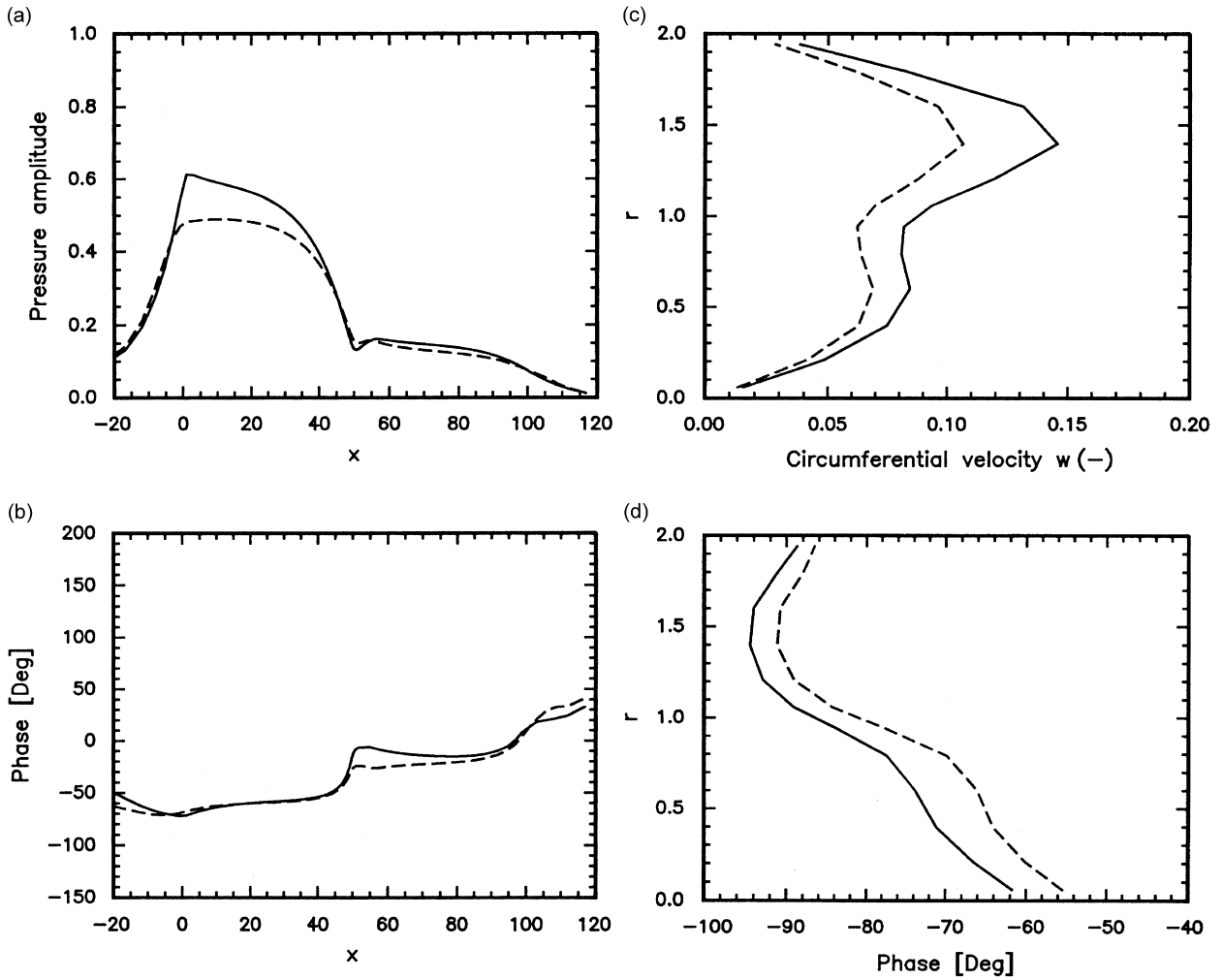


Fig. 18. (a) The non-dimensional unsteady pressure and (b) phase angle in annulus with backstep geometry for $\mathrm{Re}_{D_h} = 100$, $\omega = 0.1$, $r_{id} = 8$, $r_o = 10$ at $r = 9.942$, $\theta = 7.5°$ with $\varepsilon = 0.2$; ——, time-dependent transformation analysis; – – – –, mean-position analysis. (c, d) Circumferential velocity $w$ and phase angle at $X = 50$, $\theta = 45°$.

by the MP approach. The pressure recovery after the step is very clear, which would influence the stability of the system.

Finally, to demonstrate that the time-dependent-coordinate solution is necessary at much higher amplitudes of oscillation than the MP approach, Fig. 19 shows results for $\varepsilon = 0.5$ (for $r_i = 9.0$ and $r_o = 10.0$). It is seen that at this amplitude of oscillation there are large differences in the pressure; the phase angles nevertheless are very much closer to each other, the difference tending toward zero.

For stability analysis using the TDCT and MP models, some comparisons are made between the results of the two models. Fig. 20 presents a comparison between the displacements of the outer cylinder for $\mathrm{Re}_{D_h} = 200$ and $\omega_n = 1$ for 2-D analysis. It is seen that the TDCT analysis predicts lower damping and higher frequency of oscillation than the MP analysis, which means that the structure is more prone to instability. Fig. 21 shows a similar comparison in the behaviour of the cylinder for a less stiff structure, $\omega_n = 0.1$ and 3-D analysis. Comparison between this figure and Fig. 20 indicates that (i) less stiff structures are more damped no matter which model is used and (ii) TDCT analysis again predicts lower damping and higher frequency of oscillation for the coupled system.

Fig. 22 presents the displacement of the outer cylinder for an annular geometry with backstep. Again, the behaviour of the system is very different when the TDCT model is used. Comparison between this figure and

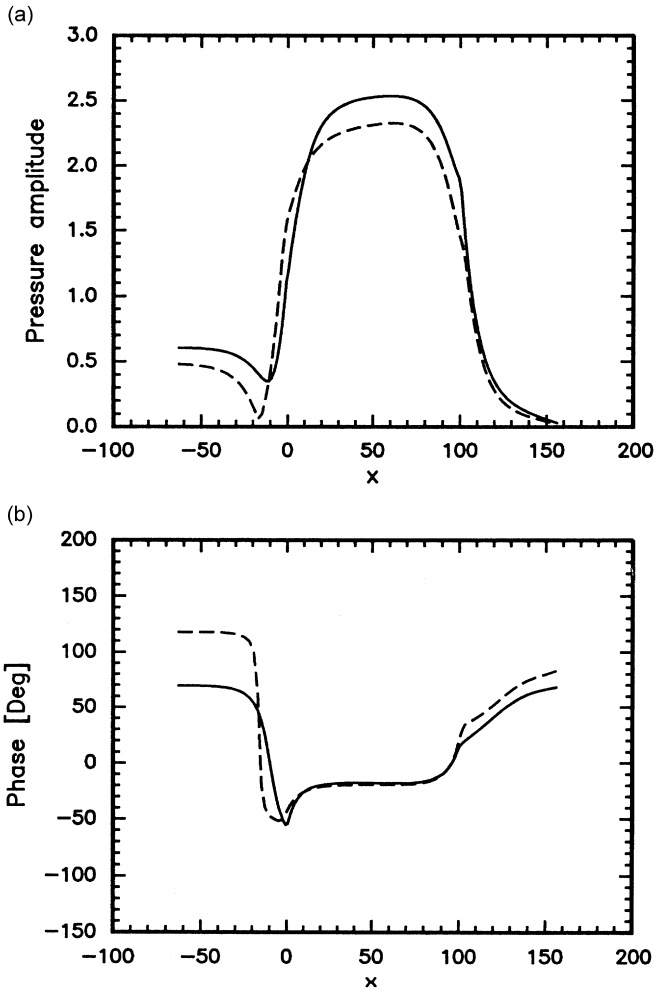


Fig. 19. (a) The non-dimensional unsteady pressure and (b) phase angle for $\mathrm{Re}_{D_h} = 250$, $\omega = 0.2$, $r_i = 9.0$, $r_o = 10.0$, $\varepsilon = 0.5$ at $r = 9.965$, $\theta = 7.5°$; ——, time-dependent transformation (TDCT) analysis; – – – –, mean-position (MP) analysis.

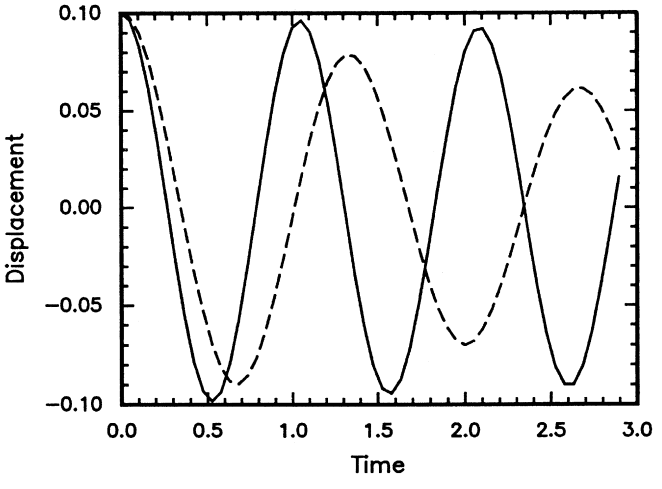


Fig. 20. Comparison between the displacements, $\varepsilon$, of the outer cylinder in translational motion versus time, $T_n = 2\pi/\omega_n$, with $\omega_n = 1$ for 2-D and $\mathrm{Re}_{D_h} = 200$: – – – –, MP analysis; ——, TDCT analysis.

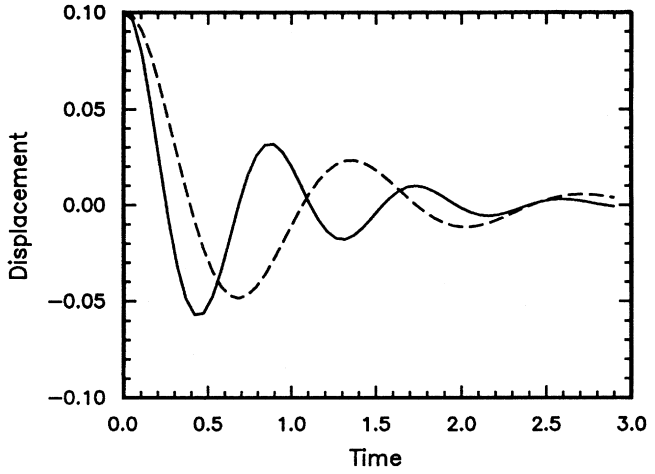


Fig. 21. Comparison between the displacements, $\varepsilon$, of the outer cylinder in translational motion versus time, $T_n = 2\pi/\omega_n$ for uniform annular geometry, with $\omega_n = 0.1$ and $\mathrm{Re}_{D_h} = 200$: – – – –, MP analysis; ——, TDCT analysis.

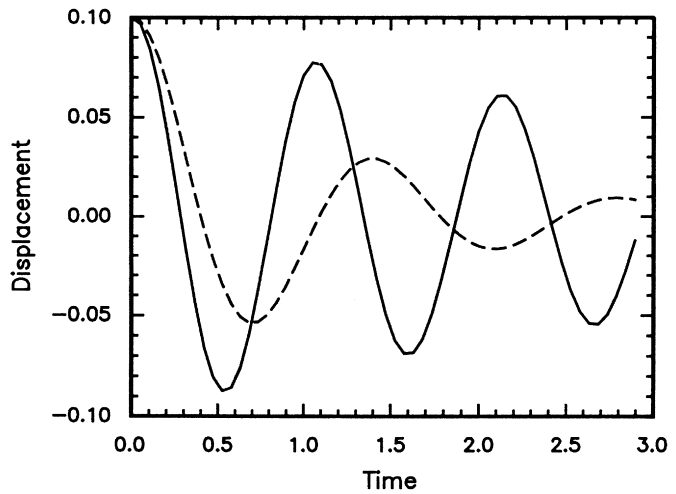


Fig. 22. Comparison between the displacements, $\varepsilon$, of the outer cylinder in translational motion versus time, $T_n = 2\pi/\omega_n$ for annular geometry with backstep, for $\omega_n = 0.1$and $\mathrm{Re}_{D_h} = 200$: – – – –, MP analysis; ——, TDCT analysis.

Fig. 21 indicates that introducing a backstep into the structure influences the stability of the system, i.e., the existence of the backstep generates a pressure recovery after the step (as shown in Fig. 18) and this pressure recovery affects the motion of the structure. Also, for the same Reynolds number and structural frequency, $\mathrm{Re}_{D_h} = 200$, $\omega_n = 0.1$, the TDCT analysis indicates a lower frequency of oscillation for the coupled system with backstep (Fig. 22) than for the system without backstep (Fig. 21).

## 5. Conclusions

The time-integration of the incompressible laminar N–S and continuity equations was effected by using the method of artificial compressibility in conjunction with a three-point backward implicit real-time differencing scheme. After the semi-discretization, artificial pseudo-time derivative terms were added to the equations, including artificial compressibility in the continuity equation. The solution was advanced from one real (physical) time level to the next by integrating in pseudo-time until steady state was reached. The equations were cast in delta-form after differencing the pseudo-time derivatives by using a Euler scheme. The solution

was effected by using the approximate factorization and ADI techniques, and finite differences were used in which the spatial differential operators were written on stretched staggered grids.

The theoretical results obtained predict the behaviour of the structure (the outer cylinder) when it is set in motion from rest. The coupling of the unsteady flow and the structural equations was effected through a predictor-corrector Runge–Kutta scheme to integrate the equation of the structure under the combined action of mechanical forces and fluid forces obtained from solving the N–S equations. The stability of the system was analyzed for (i) a 2-D (infinitely long) annular space and (ii) 3-D annular flows with different geometries and translational oscillation of the outer cylinder and (iii) uniform annular geometry and rocking motion of the outer cylinder. In the case of 2-D analysis it was shown that the outer cylinder is more stable when the Reynolds number is not very large (in the laminar regime), and that as it becomes larger the system becomes less stable. The 2-D and 3-D results obtained for uniform annular viscous flow indicate the generation of a viscosity-related added damping (which is not present for potential flow).

For a fixed Reynolds number, going from the uniform to the stepped geometry has a destabilizing effect on the system according to viscous theory (i.e. a reduction in flow-induced damping is generated). However, the system with a diffuser section is a more stable configuration than the geometry with a backward step, especially for a diffuser with a half-angle $\alpha = 6^\circ$. The diffuser with $\alpha = 20^\circ$ behaves almost like a backstep geometry, but in comparison it has a higher oscillation frequency. It is also concluded that for a uniform annular system and translational motion of the cylinder, when the natural frequency $\omega_n$ is reduced, by decreasing the spring stiffness $K$, the motions are more highly damped by fluid viscous effects, while the frequency of oscillation is reduced indicating a reduction in the stiffness of the system due to negative fluid added stiffness.[4] For a uniform annular geometry and rocking motion of the outer cylinder, the unsteady pressure and velocities generated in the annulus result in limit-cycle oscillation (flutter motion) of the outer cylinder.

To examine the effect of larger amplitude oscillations on the stability of the system, the TDCT was used to transform the N–S and continuity equations in the moving physical domain into a fixed computational domain, thereby eliminating the limitations inherent in the MP analysis. To obtain the results based on linear flow theory used by Mateescu et al. [24–26] in which the natural frequency was $\omega_n \leqslant 1$, and to compare their results with the results based on the nonlinear flow as shown in the present work by using TDCT analysis, the values of $\omega_n$ were assumed to be less than or equal to unity throughout the present analysis. Under this assumption, the results obtained using TDCT analysis indicate that the system with uniform annular geometry is more stable than predicted by MP analysis. Also, TDCT predicts less damping and higher coupled frequency of oscillation for the system. For an annular geometry with a backward step, the TDCT approach predicts much less damping than the MP analysis and a lower frequency of oscillation for the coupled system than the system without a step.

There are several features in the physics of the problems solved in the present work which are as follows:

(i) Such systems are susceptible to fluid-elastic instabilities and vibration problems, especially when the flow passage is narrow.
(ii) For the case of a rigid cylindrical body hinged at one point and coaxially positioned in a flow-carrying duct, oscillatory instability can occur at sufficiently high flow velocities, via a negative damping mechanism. The damping of the cylindrical structures due to annular flow arises from the inlet and outlet effects and from frictional effects in the annulus, both effects increasing with flow velocity.
(iii) The damping forces and pressure distribution along the annulus can be well predicted if simple assumptions about the unsteady flow in the annulus are made.
(iv) The present work is similar to the model presented by Parkin and Watson [16] for 6° and 30° annular diffusers and it is also similar to the model presented by Spurr and Hobson [12] in which the unsteady forces caused by the unsteady flow down an annulus are particularly sensitive to the amount of pressure recovery which takes place when the annulus is terminated by an annular diffuser (in the present work, by a backward step or diffuser). The pressure recovery leads to forces on the centre-body (in this work on

[4]For an annular geometry of given dimensions, as well as for a given mass, $M$, of the oscillating cylinder, only the combined (spring plus the fluid added) stiffness $K$ is changed so as to correspondingly modify the coupled $\omega_n$.

the outer cylinder) which are in phase with its velocity and therefore likely to lead to coupled fluid–structure self-excited vibrations.

(v) There are flow-induced damping (velocity-dependent) and stiffness (displacement-dependent) forces acting on the oscillatory and non-oscillatory walls.

(vi) The instability can be initiated by increasing the forced vibration amplitude, but viscous effects stabilize the system, and they become more important as the annulus becomes narrower as shown in Refs. [21,22].

(vii) By decreasing the spring constant $K$, i.e., reducing $\omega_n$, while keeping the same Re, the motion is more highly damped by fluid viscous effects.

(viii) For uniform geometry the divergence instability is obtained with $0.001 \leqslant \omega_n \leqslant 0.01$, depending on the meshes used. For the fine mesh, the system becomes overdamped and stable when $\omega_n = 0.01$ (these results have not been presented in the present work but indicate some features of the problems solved).

(ix) With a gap-width of either $h$ or $2h$ there is less damping when $\mathrm{Re} = 400$ than when $\mathrm{Re} = 200$. However, for the same Reynolds numbers, when the gap-width is $2h$ the coupled frequency of oscillation is higher.

(x) The uniform annulus results demonstrate the generation of a negative fluid-stiffness force for the lateral motions in the annulus. If the restoring (positive) spring stiffness is sufficiently small, then, for a given flow velocity, the overall stiffness may vanish, giving rise to static (divergence) instability. For the narrower annulus, the natural frequency is smaller, which means that the system is less prone to divergence (cf. Ref. [24])—at the threshold of which the sum of the mechanical and flow-induced stiffness is zero.

(xi) For non-uniform annular passages (e.g., annular passage with a backstep), when $\mathrm{Re} = 200$, $\omega_n = 0.1$, the present theory predicts a significant amount of flow-induced damping. When $\omega_n$ is one order of magnitude smaller, however, this theory predicts divergence.

(xii) Also, when the gap width is $h$ and $\mathrm{Re} = 200$ with $\omega_n = 0.01$, the system is stable, but it is unstable (by divergence) for wider uniform and stepped geometries.

(xiii) For a fixed Re, going from the uniform to the stepped geometry has a destabilizing effect on the system. This can be interpreted (a) as a larger negative stiffness being generated for a given flow velocity, or (b) the necessary flow velocity, $U$, for generating a given negative stiffness being smaller.

The final point is that, the purpose of the present calculations was, principally, to demonstrate its feasibility, and also to show some of the effects of the main system parameters on system stability, thereby gaining some physical insight into a simple but generic physical system. In this regard, it should be recalled that, throughout, the theory is for laminar flow and the motions considered are purely lateral or rocking. Hence, the temptation to relate the results to cases of flow-induced instabilities in practical systems [1] should be approached with caution.

## Acknowledgements

The support to this research by NSERC of Canada, FCAR of Québec and Bu-Ali University Research Center is gratefully acknowledged. The authors also thank Prof. D. Mateescu for his help in the course of the Ph.D. studies at McGill by the first author.

## References

[1] M.P. Païdoussis, Flow-induced vibrations in nuclear reactors and heat-exchangers: practical experiences and state of knowledge, in: E. Naudascher, D. Rockwell (Eds.), *Practical Experiences with Flow-Induced Vibrations*, Springer, Berlin, 1980, pp. 1–81.

[2] M.P. Païdoussis, *Fluid–Structure Interactions: Slender Structures and Axial Flow*, Vol. 2, Elsevier Academic Press, London, 2003 (Chapter 11).

[3] T.M. Mulcahy, A review of leakage-flow-induced vibrations of reactor components, Argonne National Laboratory Report ANL-83-43, Argonne, IL, USA, 1983.

[4] T.M. Mulcahy, Leakage-flow-induced vibrations of reactor components, *The Shock and Vibration Digest* 15 (9) (1983) 11–18.

[5] M.P. Païdoussis, Flow-induced instabilities of cylindrical structures, *Applied Mechanics Reviews* 40 (1987) 163–175.

[6] M.P. Païdoussis, M.J. Pettigrew, Dynamics of flexible cylinders in axisymmetrically confined axial flow, *Journal of Applied Mechanics* 46 (1979) 37–44.

[7] M.P. Païdoussis, M. Ostoja-Starzewski, Dynamics of flexible cylinder in subsonic axial flow, *AIAA Journal* 19 (1981) 1467–1475.
[8] M.P. Païdoussis, M.K. Au-Yang, (Eds.), *Symposium on Flow-Induced Vibrations: Vibration Induced by Axial and Annular Flows*, Vol. 4, ASME, New York, 1984.
[9] M.P. Païdoussis, M.K. Au-Yang (Eds.), *International Symposium on Flow-Induced Vibration and Noise: Axial and Annular Flow-Induced Vibration and Instabilities*, Vol. 5, ASME, New York, 1992.
[10] M.P. Païdoussis, M.K. Au-Yang, S.S. Chen (Eds.), *Symposium on Flow-Induced Vibrations: Vibration Induced by Axial and Annular Flows*, Vol. 4, ASME, New York, 1988.
[11] D.E. Hobson, Fluid-elastic instabilities caused by flow in an annulus, *Proceedings of Third International Conference on Vibration of Nuclear Plant*, Keswick, UK, 1982, pp. 440–463.
[12] A. Spurr, D.E. Hobson, Forces on the vibrating center-body of an annular diffuser, *ASME Symposium on Flow-induced Vibration, Vibration Induced by Axial and Annular Flows*, Vol. 4, ASME, New York, 1984, pp. 41–52.
[13] D.E. Hobson, Instabilities of the AGR fuel assembly during on-load refueling, in: M.P. Païdoussis, M.K. Au-Yang (Eds.), *ASME Symposium on Flow-Induced Vibration: Vibration Induced by Axial and Annular Flows*, Vol. 4, 1984, pp. 25–39.
[14] D.E. Hobson, Measurement of damping forces caused by flow between two concentric cylinders, in: *Flow Induced Vibrations*, Proceedings of the IMechE 1991–6, 1991, pp. 459–471.
[15] W.T. Ashurts, F. Durst, Studies of flow instabilities in two-dimensional test sections with sudden expansions, in: E. Naudascher, D. Rockwell (Eds.), *Practical Experiences with Flow-Induced Vibrations*, Springer, Berlin, 1980, pp. 801–808.
[16] M.W. Parkin, C.P. Watson, Reduction of vibration caused by flow in an annular diffuser, in: M.P. Païdoussis, M.K. Au-Yang (Eds.), *ASME Symposium on Flow-Induced Vibration: Vibration Induced by Axial and Annular Flows*, Vol. 4, ASME, New York, 1984, pp. 1–14.
[17] T.M. Mulcahy, One-dimensional leakage-flow vibration instabilities, *Journal of Fluids and Structures* 2 (1988) 383–403.
[18] D.E. Hobson, M. Jedwab, Investigation of the effect of eccentricity on the unsteady fluid forces on the centre-body of an annular diffuser, *Journal of Fluids and Structures* 4 (1990) 155–169.
[19] F. Inada, S. Hayama, A study on leakage-flow-induced vibrations, *Journal of Fluids and Structures* 4 (1990) 395–412 413–428.
[20] D. Mateescu, M.P. Païdoussis, The unsteady potential flow in an axially-variable annulus and its effect on the dynamics of the oscillating rigid center-body, *ASME Journal of Fluids Engineering* 107 (1985) 412–427.
[21] D. Mateescu, M.P. Païdoussis, Unsteady viscous effects on the annular-flow-induced instabilities of a rigid cylindrical body in a narrow duct, *Journal of Fluids and Structures* 1 (1987) 197–215.
[22] D. Mateescu, M.P. Païdoussis, F. Bélanger, Unsteady pressure measurements on an oscillating cylinder in narrow annular flow, *Journal of Fluids and Structures* 2 (1988) 615–628.
[23] M.P. Païdoussis, D. Mateescu, W.-G. Sim, Dynamics and stability of flexible cylinder in a narrow coaxial cylindrical duct subjected to annular flow, *Journal of Applied Mechanics* 57 (1990) 232–240.
[24] M.P. Païdoussis, D. Mateescu, F. Bélanger, A computational method for the dynamics of cylindrical structures subjected to annular flows by simultaneous integration of the Navier–Stokes and structural equations, *International Symposium on Flow-Induced Vibration and Noise: Axial and Annular Flow-Induced Vibration and Instabilities*, Vol. 5, ASME, New York, 1992, pp. 17–32.
[25] D. Mateescu, M.P. Païdoussis, F. Bélanger, Computational solutions based on a finite difference formulation for unsteady internal flows, *AIAA Paper No.* 91-0724, 1991.
[26] D. Mateescu, M.P. Païdoussis, F. Bélanger, A time-integration method using artificial compressibility for unsteady viscous flows, *Journal of Sound and Vibration* 177 (1994) 197–205.
[27] D. Mateescu, A. Mekanik, M.P. Païdoussis, Analysis of 2-D and 3-D unsteady annular flows with oscillating boundaries, based on a time-dependent coordinate transformation, *Journal of Fluids and Structures* 10 (1996) 57–77.
[28] W.Y. Soh, J.W. Goodrich, Unsteady solution of incompressible Navier–Stokes equations, *Journal of Computational Physics* 79 (1988) 113–134.
[29] A.J. Chorin, A numerical method for solving incompressible viscous flow problems, *Journal of Computational Physics* 2 (1967) 12–26.
[30] K.A. Hoffman, *Computational Fluid Dynamics for Engineers*, A Publication of Engineering Education Systems, Austin, TX, 1989.
[31] D.W. Peaceman, H.H. Rachford, The numerical solution of parabolic and elliptic differential equations, *Journal of the Society of Industrial and Applied Mathematics* 3 (1955) 28–41.
[32] J.W. Cooley, P.A.W. Lewis, P.D. Welch, The finite Fourier transform, *IEEE Transactions on Audio and Electronics* AU 17 (1969) 77–85.
[33] W.Y. Soh, Time-marching solution of incompressible Navier–Stokes equations for internal flows, *Journal of Computational Physics* 70 (1987) 232–252.
[34] F.H. Harlow, J.E. Welch, Numerical computation of time-dependent viscous incompressible flow of fluid with free surface, *Physics of Fluids* 8 (1965) 2182–2189.
[35] M. Vinokur, On one-dimensional stretching functions for finite-difference calculations, *Journal of Computational Physics* 50 (1983) 215–234.
[36] F. Bélanger, E. de Langre, F. Axisa, M.P. Paidoussis, D. Mateescu, Dynamics of coaxial cylinders in laminar annular flow by simultaneous integration of the Navier–Stokes and structural equations, *Journal of Fluids and Structures* 8 (1994) 747–770.
[37] J.F. Thompson, Z.U.A. Warsi, C. Wayne Mastin, Boundary-fitted coordinate systems for numerical solution of partial differential equations—a review, *Journal of Computational Physics* 47 (1982) 1–108.
[38] A. Mekanik, General Solution for Unsteady Annular Flows Between Concentric Cylinders and Annular Flow-induced Instabilities. Ph.D. Thesis, Department of Mechanical Engineering, McGill University, Canada, 1994.

[39] C. Benocci, P. Bellomi, V. Michelassi, Comparison of Cartesian and curvilinear grids for incompressible flow around steps, in: C. Taylor, W.G. Habashi, M.M. Hafez (Eds.), *Numerical Methods in Laminar and Turbulent Flows*, Vol. 5(Part 1), Pineridge Press, Swansea, UK, 1987, pp. 584–594.

[40] D.T. Valentine, G.W. Hyde, Axisymmetric laminar flow over an annular backstep. A numerical study, in: C. Taylor, W.G. Habashi, M.M. Hafez (Eds.), *Numerical Methods in Laminar and Turbulent Flows*, Vol. 5 (Part 1), Pineridge Press, Swansea, UK, 1987, pp. 607–618.

[41] F. Bélanger, M.P. Païdoussis, E. de Langre, Time-marching analysis of fluid-coupled systems with large added mass, *AIAA Journal* 33 (1995) 752–757.